From atoms to aerosols: Probing clusters and nanoparticles with synchrotron based mass spectrometry and X-ray spectroscopy

Journal:	*Physical Chemistry Chemical Physics*
Manuscript ID	CP-PER-10-2019-005802.R1
Article Type:	Perspective
Date Submitted by the Author:	09-Jan-2020
Complete List of Authors:	Ahmed, Musahid; Lawrence Berkeley National Laboratory, Chemical Sciences Division Kostko, Oleg; Lawrence Berkeley National Laboratory, Chemical Sciences Division

From atoms to aerosols: Probing clusters and nanoparticles with synchrotron based mass spectrometry and X-ray spectroscopy

Musahid Ahmed* and Oleg Kostko

Chemical Sciences Division, Lawrence Berkeley National Laboratory

Berkeley, CA-94720, USA

* mahmed@lbl.gov

Abstract

Tunable synchrotron radiation provides a universal, yet selective scalpel to decipher molecular information in complex chemical systems when coupled to mass spectrometry and X-ray spectroscopy. At the Chemical Dynamics Beamline, the radiation emanating from the Advanced Light Source at Berkeley has been utilized by physical chemists and chemical physicists to probe chemical reactivity, energetics and spectroscopy for over two decades. Emerging themes are the study of molecular growth mechanisms, solvation, electronic structure and reactivity in clusters, complexes and nanoparticles. The ion-induced and neutral growth mechanisms in methanol and acetylene clusters are revealed by vacuum ultraviolet (VUV) single photon ionization mass spectrometry. The photoionization dynamics of glycerol show signatures of strong ionic hydrogen bonds, non-covalent interactions are explored in naphthalene water clusters, proton transfer pathways are revealed in acetaldehyde water clusters, and exciton charge transfer is probed in argon water clusters. X-ray spectroscopy provides a local probe of a sample’s electronic structure with elemental and site-specificity and is thus ideally suited for probing solvation. Velocity map imaging X-ray photoelectron spectroscopy coupled to nanoparticle beams that allows for the visualization of dynamic processes in solvation and molecular growth processes is described. This technique is used to probe reactivity in aerosol chemistry, obtain phase and pH dependent information on aqueous nanoparticles and electron scattering cross-sections from hydrocarbon nanoparticles. We describe future opportunities in probing elusive radicals such as the cyclic 3,5-dehydroxyphenyl radical cation and excited states in water clusters formed in VUV photoionization, explore reactivity in confined spaces via X-ray spectroscopy and elucidate time dynamics with laser-synchrotron pump probe experiments.

Introduction

Physical Chemistry and Chemical Physics are science disciplines that have endeavored to bring a molecular-level understanding to complicated processes, relevant to energy production and climate change, such as combustion chemistry and reactions in microscopic environments within atmospheric aerosols. In this perspective we provide a glimpse of how a beamline at a synchrotron devoted to chemical dynamics is being utilized to provide insight in this direction. Chemical dynamics at Lawrence Berkeley National Laboratory (Berkeley Lab) has had a long and distinguished history, culminating in the Nobel Prize in Chemistry to Yuan T. Lee for developing chemical reaction dynamics in crossed molecular beams. In 1994, Lee moved back to Taiwan, however he sowed the seeds of a program (under the stewardship of Arthur Suits, Cheuk Ng, Thomas Baer, and Stephen Leone) which has moved the beamline from probing elementary reactions and high resolution spectroscopy in the gas phase to studying complexity in clusters, aerosols and nanoparticles using vacuum ultraviolet (VUV) and soft X-ray radiation, generated at a synchrotron.

In this perspective, we provide snapshots of this science, gathered over work performed in the last 5 years and point towards future exciting directions in the field. All of the work described here has been performed at the Advanced Light Source (ALS), a third generation synchrotron located within the environs of Berkeley Lab. The chemical dynamics beamline (beamline 9.0.2) has historically been a place for the development of unique instrumentation and methods to probe complex chemical kinetics and dynamics using tunable VUV radiation and mass spectrometry in the gas phase. A review of this work has been published recently,[1] and earlier reports describes the origin and history of this particular beamline.[2, 3] With the acquisition of new hardware, this beamline now has a dedicated port for soft X-rays, and we hope to show in this perspective, that a seamless transition is occurring in the science and methods employed in probing chemical dynamics and reactivity from the gas to the condensed phase. While we focus on using synchrotron radiation to probe chemical transformations in clusters and nanoparticles, the interested reader may find recent reviews of spectroscopy and dynamics of molecules and clusters,[4] ultrafast X-ray probing in chemical dynamics[5], and the study of clusters and nanoparticles at a free electron laser (FEL)[6] illuminating and can act as a contrast to science that is being performed with a 25 year old instrument.

The structure of the paper is as follows, we start with a brief description of the beamline and instrumentation, followed by our work on using VUV based molecular beam mass spectrometry to probe clusters in the gas phase, transitioning to a combined mass spectrometry and valence band photoelectron spectroscopy study of aqueous aerosols, and culminating on development and implementation of soft X-ray velocity map imaging (VMI) of nanoparticles. We benefit from theoretical insight to these problems, particularly at the valence level, and these studies are highlighted in this paper.

The Chemical Dynamics Beamline and instrumentation

The beamline (Figure 1) is comprised of an undulator which produces tunable radiation spanning from the VUV to soft X-rays. With a combination of mirrors and gratings, light in the range between 7.4-25.4 eV, is directed to four terminals, which allow access to roll on – roll off instrumentation. Two of the terminals are monochromatized allowing for medium resolution (10-50 meV). The cluster science using molecular beam mass spectrometry described here was performed at terminal 4 (T4 in Fig. 1). The aerosol based mass spectrometry instrument is located at terminal 2 (T2), where the full beam is utilized using the natural tunability of the undulator and resolution (~ 0.34 eV) to generate threshold photoionization mass spectra. In 2014, with the decommissioning of the National Science Foundation funded synchrotron at Wisconsin, we procured and installed in cooperation with the ALS, a state of the art soft X-ray beamline, which now provides soft X-rays in the range of 15-800 eV, with photon fluxes of around 10^{12} photons/s at a notional resolving power (E/ΔE) of 5000. At present there is one terminal, and another will be installed in the foreseeable future. The beamline also benefits from access to high repetition rate and CW lasers for multimodal interrogation of systems with Raman, THz, and IR radiation.

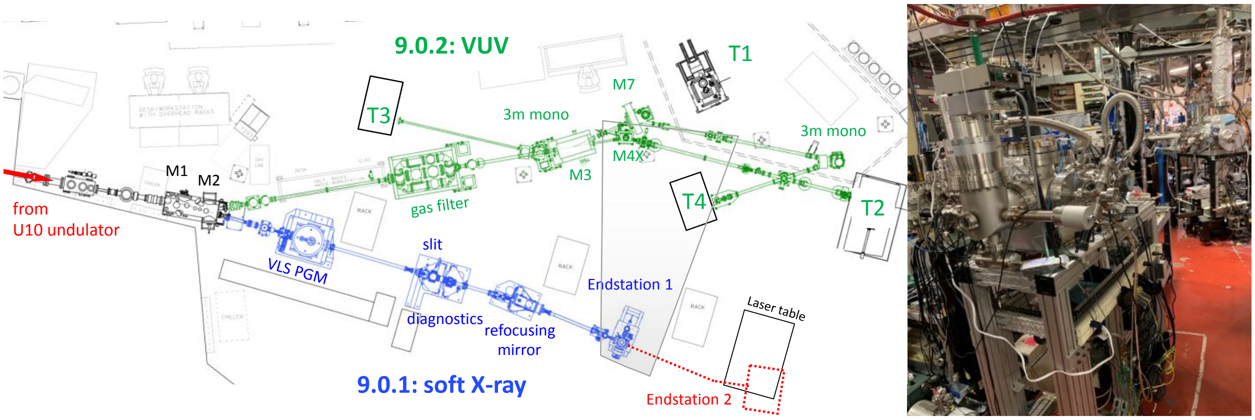

Fig. 1. A layout of the chemical dynamics beamline. The green section shows the hardware for VUV delivery between 7.4-25.4 eV; the blue section shows the soft X-ray part delivering photons between 15-800 eV. The red section will be commissioned in the future. The picture on the right shows the velocity map imaging spectrometer in the foreground located at the soft X-ray terminal, and the molecular beams machine in the background at T4. Field of view is highlighted on the beamline schematic.

The cluster molecular beam apparatus[7] is 19 years old, and is designed to accept different sources to generate species for subsequent photoionization and detection using an RM Jordan reflectron mass spectrometer (Fig. 2a).[8] Laser ablation and reaction of metal,[9, 10] carbon[11] and silicon clusters,[12, 13] hot nozzle reactions of radicals and molecules leading to polycyclic aromatic hydrocarbons,[14-22] and even a mini shock tube[23] to examine high temperature and pressure reactions have utilized this instrument. For the work described here, a CW nozzle with variable openings, coupled to different sublimation sources have been adapted to generate various complexes and clusters. For the ion-molecule clustering reactions, ion optics were inserted into the source region to allow transport of the resulting ions to the mass spectrometer as well as differential pumping was incorporated to allow direct access to the synchrotron radiation into the source region (Fig. 2b).[24] A recent innovation has been use of a microfluidic device at the ionization region of the mass spectrometer.[25] This device, which has a tiny orifice (2-3 microns), allows for sampling directly the gas phase molecules emanating from the liquid underneath, while maintaining vacuum in the mass spectrometer. We have applied this method to probe phase changes in ionic liquids[26] and dynamic electrochemistry in a Li_2S_8 battery.

Two decades ago, around the same time that we developed the molecular beams apparatus, we embarked on a program to probe aerosols and nanoparticles with synchrotron based VUV radiation. We adapted a crossed molecular beam instrument to incorporate an aerodynamic lens system, to focus nanoparticles into the interaction region. Upon impinging on a hot plate within the environs of the ion optics, the aerosols would vaporize and the gas phase molecules would be ionized via synchrotron radiation.[27] Initially the ions were detected with a linear time of flight (TOF) mass spectrometer, however subsequently an orthogonal TOF mass spectrometer was introduced resulting in much higher resolution and stability of the ion beam. Recently the apparatus was coupled to a flame sampling apparatus,[28] allowing for the identification of new radical pathways in molecular growth processes relevant to combustion (Fig. 2c).[29] The original instrument was also equipped with velocity map imaging optics, which allowed detection of photoelectrons and was used to perform valence level photoelectron spectroscopy of biological nanoparticles.[30]

In 2014, we started to incorporate soft X-rays to the beamline, and simultaneously built a second generation velocity map imaging photoelectron spectrometer coupled with the aerodynamic lens to allow probing of unsupported nanoparticles (NP) (Fig. 2d).[31] We designed the optics to capture photoelectrons with up to 100 eV kinetic energy, hence would be amenable to soft X-ray probing of core level electrons. The instrument was easily transportable between various beamlines, and the work described later was performed on four such beamlines at the ALS. The instrument is designed in such a way so that laser radiation can be incorporated in tandem with synchrotron radiation, and future improvements will be to incorporate detectors for measuring X-ray scattering simultaneously. Again we benefit from knowledge acquired decades ago on performing Mie scattering from silica nanoparticles with VUV radiation.[32]

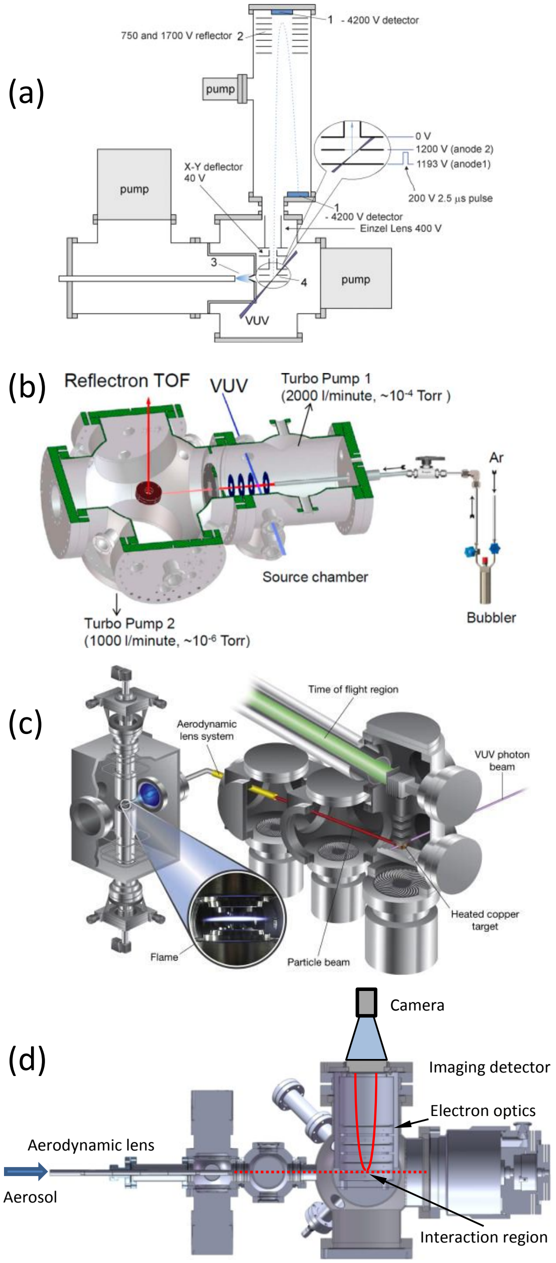

Fig. 2. Schematics of end stations used to probe clusters and nanoparticles: (a) molecular beam apparatus. (b) The apparatus depicted in (a), is adapted for ionization in the source region. Reprinted with permission from ref. 24. Copyright (2015) American Chemical Society. (c) The aerosol mass spectrometer coupled to a flame sampling apparatus. Reprinted from ref. 28 with permission from Elsevier. (d) Nanoparticle sampling velocity map imaging photoelectron spectrometer. Adapted with permission from ref. 31. Copyright (2017) American Institute of Physics.

VUV photoionization dynamics in clusters

The photoionization dynamics of clusters is of paramount interest in a number of fields spanning biology, chemistry, and physics.[33, 34] Understanding the changes in electronic structure that occur in the ionic clusters is critical to unveil their structure and function and is important in cloud nucleation in the earth's atmosphere,[35] radiation biology,[36] and catalysis.[37] Furthermore, they can act as model systems for understanding non-covalent interactions[38] and their effects on chemical reactivity, for instance in heterogeneous catalysis,[39] ionic liquids,[40] and aerosol chemistry.[41] We have investigated proton and charge transfer in hydrogen bonded, π-stacked and solvated systems using synchrotron based molecular beams mass spectrometry coupled with electronic structure calculations performed within the group and also with extensive collaborations with Martin Head-Gordon (UC Berkeley) and Anna Krylov (USC). Below we describe work performed over the last five years, the earlier work is documented in a recent review.[1]

Ion and neutral growth pathways in methanol clusters, and in acetylene-ethylene clusters

Nucleation is a phenomenon generally defined as formation of molecular embryos during vapor – liquid – solid phase transitions.[42] Small neutral molecules and ions can act as nucleating species which typically play key roles in molecular growth and can have profound implications, such as cloud formation.[43] We have recently developed an experimental strategy for characterizing neutral versus ion-induced growth using in-source ionization of molecular beams with tunable VUV synchrotron radiation. Methanol was chosen as a model system, since we had previously studied its neutral growth processes in molecular beams.[44] Using the apparatus, shown in figure 2b, we could vary the distance between ionization and the nozzle. The mass spectral distributions of the ionized clusters and their products show signatures for both ion-induced and neutral growth (Fig. 3).

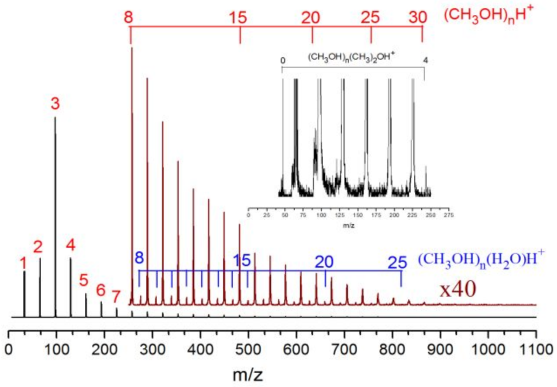

Fig. 3. Mass spectrum showing various cluster distributions measured at an ionization distance of 10 mm from the nozzle at 11 eV photon energy. Insets show an expanded view of protonated methanol and methanol-dimethyl ether distributions. Reprinted with permission from ref. 24. Copyright (2015) American Chemical Society.

Protonated methanol clusters, protonated methanol-water clusters, and protonated methanol-dimethyl ether clusters were observed, and the intensity distribution for protonated methanol is shown on the bottom panel of figure 4. Using appearance energy measurements for the various species to decipher whether the clusters are formed by ion or neutral collision pathways, coupled to fluid dynamics calculations of the supersonic expansion, we could use Thomson's liquid drop model to explain the intensity distributions shown in upper panel of figure 4.[24] Thomson's model is based on the thermodynamics of a liquid drop at equilibrium, which uses bulk variables such as surface tension and dielectric constants. While it is suspect to derive quantitative information for clusters using this model, it does provide a qualitative value and informs us about what mechanisms are operational. At closer distances, both super-saturation and ion-induced growth mechanisms reduce the free energy of formation. In contrast, low neutral density of the molecules at the further distances increase the free energy barrier, reducing the ion-induced growth processes. Very recently Lietard and Verlet[45] studied the selectivity in electron attachment to water clusters by varying the ionization distance from the nozzle, reminiscent of the method employed here. We have also observed non-equilibrium distributions of water clusters upon nozzle to ionization distance changes, and preliminary analysis suggests that ion-induced growth dominates near the nozzle.

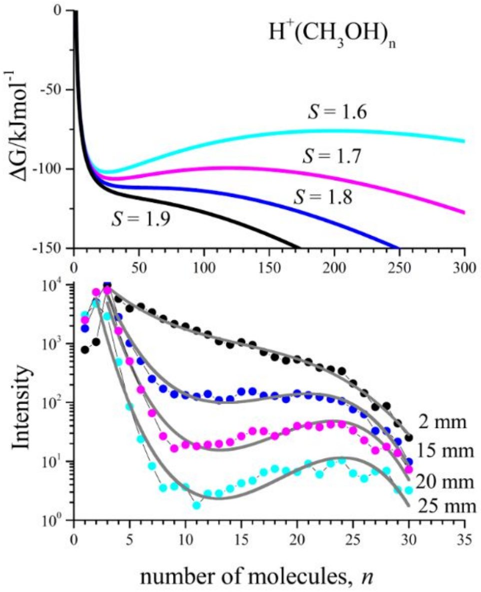

Fig. 4. Free energy of formation (ΔG) as a function of number of molecules (n) and different super-saturation ratios (S) according to Thomson's liquid drop model. Intensity distributions of protonated methanol measured at distances 2, 15, 20, and 25 mm. Reprinted with permission from ref. 24. Copyright (2015) American Chemical Society.

Ion-molecule reactions[46] as well as neutral radical reactions[47] in hydrocarbon systems is of importance in astrochemistry, where it is believed that these reactions lead to polycyclic aromatic hydrocarbon (PAH) formation across the interstellar medium. PAH growth processes are also very important in combustion chemistry[14, 20, 22, 48] as they are precursors for soot formation.[49] With the advent of nanomaterials based on graphene, [50] fullerenes,[51] and carbon nanotubes,[52] there is also increased interest in the formation of these materials from their gas phase precursors. To elucidate ion-molecule growth dynamics in hydrocarbons, we chose mixed acetylene-ethylene clusters[53] and pure acetylene clusters.[54] The experimental set up essentially has two controls - one can tune the photon energy to precisely ionize a moiety and secondly, change the ionization distance to probe various regions of an expansion as demonstrated earlier with methanol. This work focused mainly on the formation of $(C_2H_2)(C_2H_2)$, $(C_2H_2)(C_2H_4)$, and $(C_2H_4)(C_2H_4)$ dimers. In collaboration with Martin Head-Gordon, we used density functional theory (ωB97X-V/aug-cc-pVTZ) to study the structures and energetics of the neutral and ionized dimers. Furthermore, we have studied the possible isomerization processes and from that obtained mechanistic insight into reaction pathways as a function of nozzle to ionization region distance. For $C_4H_4^+$, possible fragmentation channels are H or H_2 loss. Energetically both channels are possible. Fragmentation from $C_4H_8^+$ and $C_4H_6^+$ includes hydrogen-loss and methyl radical loss channels. While different isomers on the potential energy surface (PES) are accessible, it is the isomerization rate that dictates fragmentation. A notable discovery from inspection of the PES's was that covalently bound cyclic isomers could be present, and these could be precursors for PAH formation.

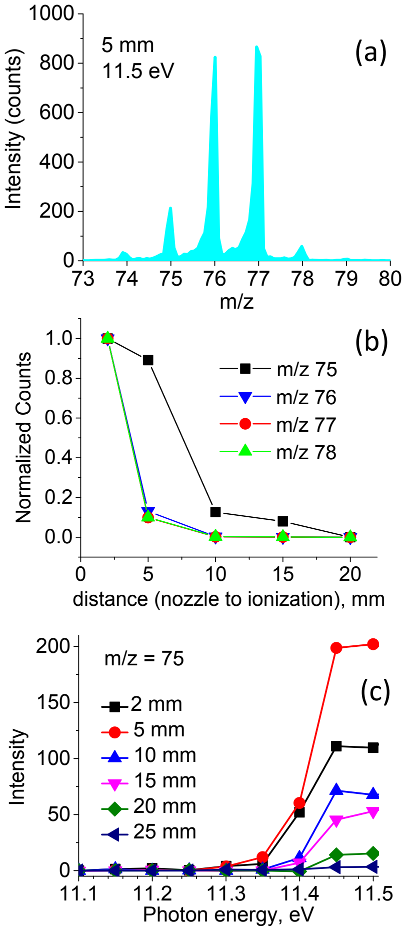

Fig. 5 (a) Mass spectrum between m/z 73-80, measured at 5 mm distance between nozzle and ionization at a photon energy of 11.5 eV from ionization of an acetylene expansion. (b) Normalized ion counts for m/z 75, 76, 77, and 78 as a function of nozzle to ionization distance at 11.5 eV photon energy. (c) Photoionization efficiency curves (PIE) for m/z 75 at various nozzle-ionization distances.

Another tantalizing experimental finding was the presence of m/z 75 in a pure C_2H_2 expansion as shown in figure 5a. This spectrum was measured at 11.5 eV photon energy with a pure acetylene expansion in argon, and could arise from unimolecular decomposition of a larger acetylene cluster, or from association of an ionic moiety with neutral acetylene. By tracking this mass vs nozzle to ionization distance shown in figure 5b, it would suggest that this occurs from unimolecular decomposition at distances of ionized acetylene clusters beyond 5 mm, given the large drop in intensity. Contrast this with the other masses nearby at m/z 76, 77, and 78 which drops intensity dramatically beyond the 2 mm distance. What could be so special about m/z 75? Its appearance energy as a function of distance, shown in figure 5c is around 11.3-11.4 eV, suggesting its origin could be from reaction of an ion which has an onset around that region, or from unimolecular decomposition of a cluster ion with a barrier. For instance, appearance energies

(AE) of C_2H_2, $(C_2H_2)_2$, and $(C_2H_2)_3$ in our experiment are 11.3, 10.8, and 10.2 eV, respectively. In 1984, Schleyer et al.[55] postulated the 3,5-dehydroxyphenyl radical cation might be stable due to its double aromaticity conferred by the presence of two (4n+2) electrons. Following on, Head-Gordon and coworkers have looked at the formation and stability of various $C_6H_3^+$ isomers particularly under hydrocarbon plasma conditions relevant to astrochemistry.[56] They postulated that internal energies of a vibrationally hot product could be dissipated by unimolecular decomposition of a hot complex, reminiscent of what was described earlier. Perhaps our m/z 75 ion is the cyclic isomer, long postulated and never observed in experiment. Coupling VUV photoionization to IR spectroscopy as demonstrated by Fujii and coworkers might be a way to confirm the identity of m/z 75.[57]

From van der Waals to covalent bonding in ionized acetylene clusters

Ever since Berthelot observed aromatic molecules in 1867 upon heating acetylene,[58] the formation of the first ring (benzene) from acetylene clusters has served as a model for the study of molecular growth processes in hydrocarbon systems. Using a variety of molecular beam methods coupled to vacuum ultraviolet radiation,[59, 60] electron impact ionization,[61-63] and vibrational predissociation spectroscopy[64] for over 40 years, a picture has emerged on the first molecular pathways that lead to benzene formation from acetylene. Guided by these earlier results, we now focus on the decomposition mechanisms of larger acetylene clusters leading to ring formation.[54] This is illustrated in figure 6, where ion-molecule reactions with in-source ionization can lead to fragmentation products. Notice the absence of m/z 52 and 78, which are acetylene dimer and trimer respectively. However, the products change from reactive fragmentation products in a higher temperature, higher density gas regime towards a very cold collision-free cluster regime that is dominated by products, whose empirical formula is $(C_2H_2)_n^+$, just like ionized acetylene clusters. The fragmentation products result from reactive ion-molecule collisions in a comparatively higher pressure and temperature regime followed by unimolecular decomposition. The system displays rich dynamics, the neutral structures are dominated by CH-π interactions which rearrange upon ionization to those that contain bonded $C_4H_4^+$ and $C_6H_6^+$ structures solvated with one or more neutral acetylene molecules. Such species contain large amounts (above 2 eV) of excess internal energy. The role of the solvent acetylene molecules is to affect the barrier crossing dynamics in the PES between $(C_2H_2)_n^+$ isomers and provide evaporative cooling to dissipate the excess internal energy and stabilize products including the aromatic ring of the benzene cation. Formation of the benzene cation is demonstrated in ab-initio molecular dynamics (AIMD) simulations of acetylene clusters with $n>3$, as well as other metastable $C_6H_6^+$ isomers. The simulations reveal that it is not enough for ring structure (the benzene cation) to cross the entrance barrier, there needs to be an effective way of dissipating the excess internal energy beyond radiative relaxation. The PES for benzene formation from the acetylene tetramer upon ionization is shown in Fig. 7. Associated snapshots also reveal the time dependent dynamics of bond formation. We posit that such structures could perhaps be accessed by an ultrafast VUV FEL coupled to infrared spectroscopy as is being developed in the group of Ling Jiang at the Dalian Institute of Chemical Physics, China.

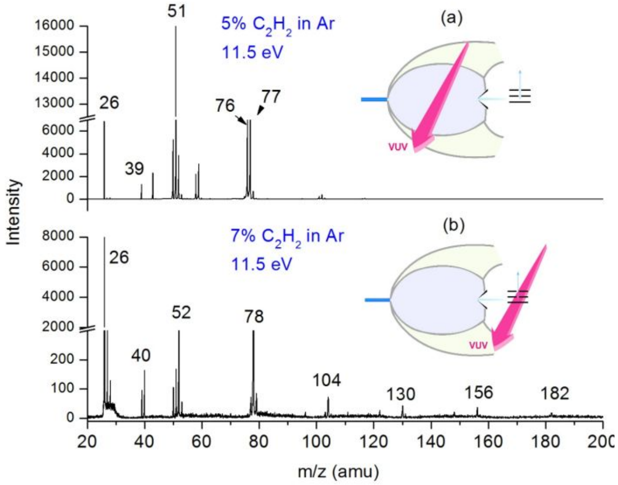

Fig.6. Mass spectra of acetylene clusters obtained from in-source (a) and mass spectrometry ionization (b) at 11.5 eV. The experimental schemes are graphically shown in the insets. Whereas in-source ionization shows fragmented acetylene clusters (e.g., $C_4H_3^+$, $C_6H_5^+$), mass spectrometry ionization shows intact clusters in the form of $(C_2H_2)_n^+$. Reproduced from ref. 54 with permission from National Academy of Sciences, copyright 2017.

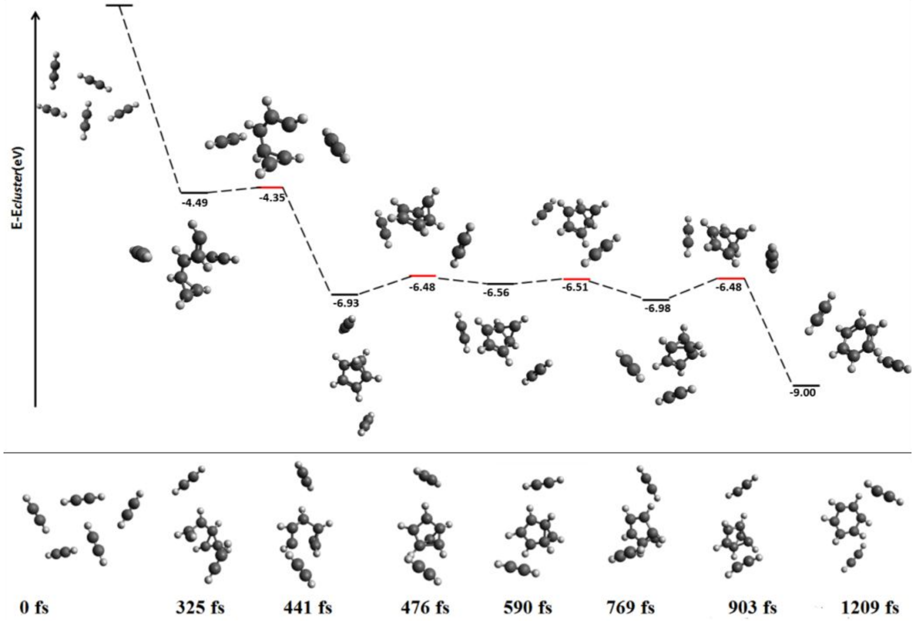

Fig. 7 (Top) Stationary points (saddle points in red) on a pathway leading to benzene cation from the ionized tetramer cluster. Relative energies (electron volts) of the different structures are with respect to the initial cluster geometry. (Bottom) Snapshots from a trajectory leading to benzene cation formation from the tetramer cluster. Reproduced from ref. 54 with permission from National Academy of Sciences, copyright 2017.

Non-covalent interactions and photoionization dynamics

Non covalent interactions such as hydrogen bonding, electrostatics, and van der Waals forces play a crucial role in driving chemical reactivity particularly in liquids – typically where most synthesis occurs.[65] Water as a solvent occupies a unique space here, and these subtle forces acting out on complicated potential energy surfaces on a multitude of time scales and distances, drive the final outcome of a chemical reaction.[66, 67] For example, supramolecular chemistry is governed by a subtle interplay of non-covalent interactions between molecules, which gives rise to the formation of intricate self-organized chemical structures.[68] These processes were thought to be mostly driven by thermodynamics, but we now know that kinetics can be a determining factor, *i.e.,* the selectivity and yield are dictated by the reaction pathway instead of the free energy of the product. Clusters involving non-covalent interactions can be used as a vehicle for studying molecular properties,[69] on theoretically tractable potential energy surfaces and electronic structure calculations, allowing for systematic investigations of how bulk properties of a substance arise from the single molecule as the number of molecules is increased.

Strong ionic hydrogen bonds in glycerol

We have developed a program in application of VUV photoionization and theoretical calculations in deciphering kinetics, dynamics and photo-induced reactivity of molecular clusters, especially hydrogen-bonded and van der Waals clusters. Our studies, with theoretical support from Anna Krylov on water clusters,[70] nucleic acid base clusters[71-73] and their complexes with water clusters[74, 75] provided signatures of proton transfer induced by photoionization in hydrogen-bonded and π-stacked systems. This work has been reviewed recently,[1] and here we will discuss new work that we have embarked on in the last few years. Due to the unquestioned importance of water in biological[76] and atmospheric [35] processes on Earth and in astrochemistry,[77] we continue the study of photon-induced reactivity of non-covalent-bonded water-containing clusters at the molecular level. A recurring theme in the ionization of these hydroxyl rich systems are the “ionic hydrogen bonds”, a special class of hydrogen bonds, which form between (radical) ions and neutral molecules.[78] Their bond strengths exceed those of a typical hydrogen bond by far and lie between 5 and 35 kcal/mol. “Ionic hydrogen bonds” are proposed to play a key role in biology and chemistry, such as protein folding, enzyme activity, biomolecular recognition and sensors, surface adsorption, self-assembly in supramolecular chemistry and molecular crystals, electrolytes, ion solvation, and ionic clusters.

Initially we focused on studying the photoionization dynamics of glycerol, which contains three hydroxyl groups and is miscible with water and its dimer, followed by glycerol-water and naphthalene-water as prototypical models for hydrophilic and hydrophobic interactions, respectively. Glycerol is a key molecular building block of lipids and can be used as a cryo-protectant to stabilize molecules, cells and tissues under cooling to subzero temperatures. As a result, it plays important roles in biotechnology, plant and animal breeding, the pharmaceutical industry, and modern medicine. While the physical properties of glycerol and its interactions with water have been studied extensively, the H-bond patterns of glycerol-water mixtures are much less reported at a molecular level. Neutron scattering[79] and molecular dynamics simulations[80] suggest that glycerol and water form clusters depending on mixing ratios which is directed by intramolecular and intermolecular hydrogen bonding between the two systems. Very recently a hypothesis connecting the freezing of aqueous solutions and chemical stability of amorphous pharmaceuticals have invoked water clusters,[81] and the aforementioned neutron scattering and molecular dynamics calculations were used as evidence in this intriguing suggestion.

The photoionization and dissociative photoionization of glycerol and its dimer were studied with photoionization mass spectrometry coupled with isotopic labelling to investigate the nature of the major fragments and their corresponding appearance energies.[82] The mass spectra are complex as shown in figure 8. We used an effusive source to generate only the glycerol monomer, and upon supersonic expansion through a nozzle, cluster formation commenced. Seeding the Ar carrier gas with water led to the formation of glycerol-water clusters. To understand the fragmentation dynamics, we initiated a collaboration with Martin Head-Gordon. It was discovered that the primary fragmentation of the glycerol radical cation occurs only via two routes.

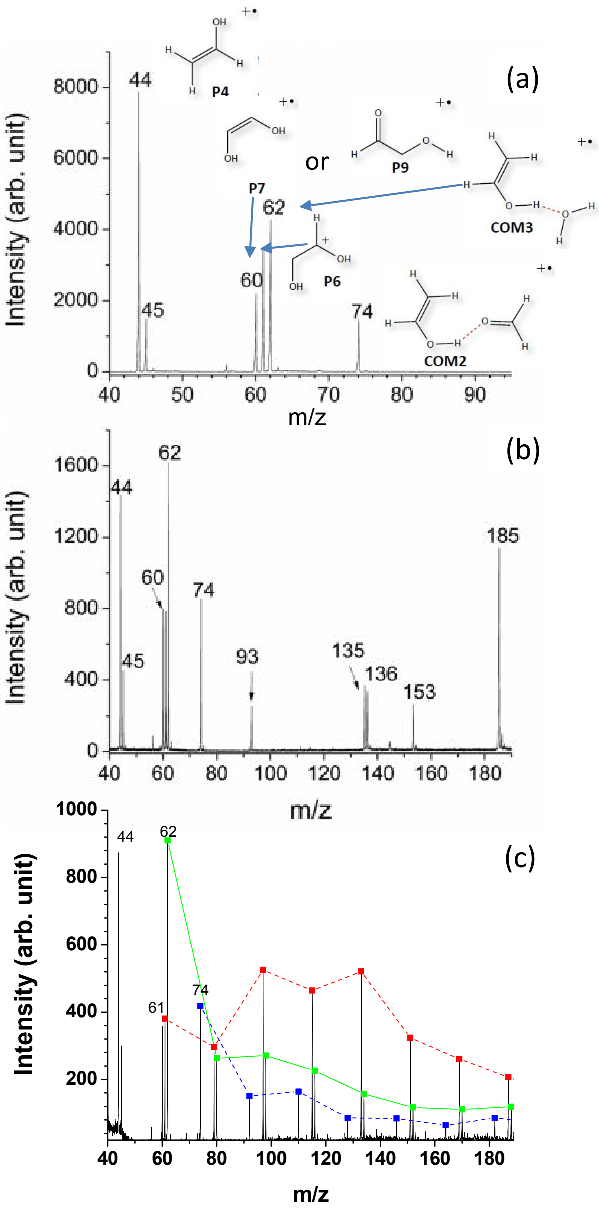

Fig. 8. Mass spectra at 10.5 eV of (a) glycerol from an effusive source, (b) glycerol from a supersonic expansion, (c) supersonic expansion of glycerol and water. In (c) red depicts mass peak series for m/z 61 $(H_2O)_n$, green depicts m/z 62 $(H_2O)_n$, and blue depicts m/z 74 $(H_2O)_n$. (a) and (b) adapted with permission from ref. 82. Copyright (2013) American Chemical Society.

The first channel proceeds via a six-membered hydrogen-transfer transition state leading to a common stable ternary intermediate (COM1) - comprised of neutral water, neutral formaldehyde, and a vinyl alcohol radical cation, which exhibits a binding energy of about 42 kcal/mol and a very short (1.4 Å) H-bond (Fig. 9). Fragmentation of this intermediate gives rise to experimentally observed ion fragments, some of which consist of "ionic hydrogen bonds". The second fragmentation route arises from cleaving the elongated C−C bond. Also for this channel, intermediates comprised of ionic hydrogen bonded complex exhibiting binding energies above 24 kcal/mol are observed. We would like to point out that an earlier study from our group on deoxyribose photoionization coupled with a theoretical analysis, also showed the cleavage of an elongated C-C bond.[83] In deoxyribose, it is the unfurling of a cyclic neutral structure upon ionization which drives the fragmentation dynamics.

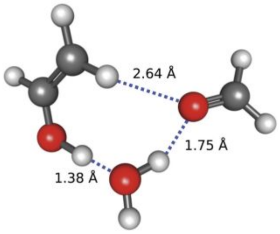

Fig. 9. The COM1 complex comprised of neutral water, neutral formaldehyde, and the vinyl radical cation. Reproduced from ref. 84 with permission from the PCCP Owner Societies.

To further understand the nature of these ionic hydrogen bonds which seem to be driving the fragmentation patterns observed, energy decomposition analysis (EDA) was employed, revealing that electrostatic and charge-transfer interactions are equally important in hydrogen-bridged ion−molecule complexes. In contrast to what was supposed to be ion-dipole interactions, EDA revealed that about ½ of the interaction energy is associated with charge transfer. This analysis has recently been confirmed with a second generation EDA[84] using absolutely localized molecular orbitals showing how non-covalent interactions can be studied by photoionization mass spectrometry. Guided by an understanding of the fragmentation patterns of the monomer, we then looked at the dimer, a first step in developing a molecular understanding of the intermolecular hydrogen bonding network known to exist in glycerol.

From an extensive conformer search, we identified a number of structures, the lowest is shown in figure 10a, where intermolecular hydrogen bonding dominates. A spin density analysis of the ionized dimer suggests that all the density is on one monomer (Fig. 10b), with the other just acting as a spectator. The fragmentation patterns for the dimer radical cation can be described as a glycerol radical cation in the presence of a spectator glycerol, thus giving rise to a dissociation pattern similar to that of the monomer. However, the spectator glycerol lowers the barrier affiliated with separating the resulting products (water, formaldehyde, and a vinyl alcohol cation) as it aids the delocalization of positive charge and spin density and no water or formaldehyde loss is observed from the dimer as can be seen in figure 8. Ongoing work in our group on glycerol-water mixtures suggest that water can dramatically change the fragmentation patterns of glycerol photoionization (figure 8c) and theory from the Head-Gordon group is beginning to shed light on how these two systems disrupt each other's hydrogen bonding network. A new direction would be to probe the VUV photoionization dynamics of such species with ultrafast spectroscopies, either with IR or X-rays which would provide signatures of hydrogen bond dynamics suggested by our very static fragmentation patterns and illuminated by the corresponding theoretical calculations.

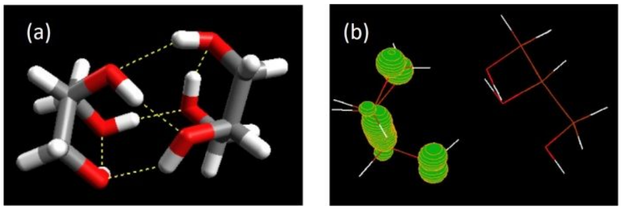

Fig. 10. (a) Cartoon of the lowest energy dimer structure, highlighting the hydrogen bonding network. (b) Spin density in glycerol dimer radical cation. Reprinted with permission from ref. 82. Copyright (2013) American Chemical Society.

Proton transfer pathways in acetaldehyde water clusters

Hydrogen bonding typically acts as a conduit for proton transfer,[85] and is crucial for driving chemical reactions, and is relevant in biological systems, electrochemistry and atmospheric photochemistry.[86] In today's world, where carbon-free energy generation processes and access to clean water are driving the scientific endeavor, an understanding of proton transfer mechanisms in membranes[87] and fuel cells is also important. We used acetaldehyde-water clusters photoionization to probe the nature of these processes.[88] VUV photoionization of an acetaldehyde-water expansion generated a series of protonated acetaldehyde and protonated acetaldehyde water clusters (Fig. 11).

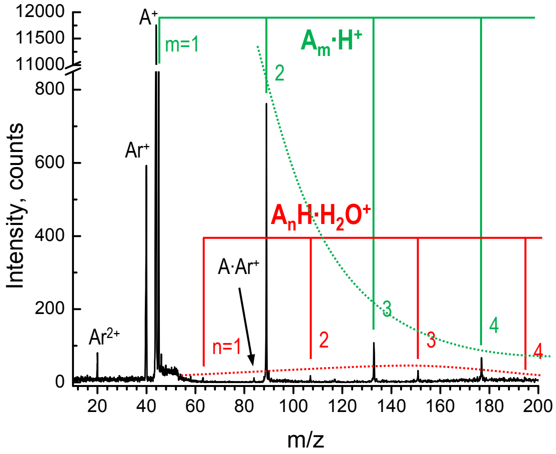

Fig. 11. Photoionization time-of-flight mass spectrum of acetaldehyde–water complexes (A_mH^+ and $A_nH{\cdot}H_2O^+$), measured at 10.5 eV photon energy. Two series of peaks detected in the experiment are color coded: green corresponds to protonated bare acetaldehyde clusters (A_mH^+), red peaks represent protonated acetaldehyde–water ($A_nH{\cdot}H_2O^+$) complexes. Dashed lines demonstrate intensity trends for A_mH^+ and $A_nH{\cdot}H_2O^+$ species. Ar^+ and Ar_2^+ peaks appear due to high harmonic ionization of argon which is used as carrier gas. The small peak at m/z 84 corresponds to the acetaldehyde–argon ion complex. Reproduced from ref. 88 with permission from the PCCP Owner Societies.

We then undertook electronic structure calculations to decipher the appearance of certain mass peaks at various photon energies, and in figure 12 we show the relevant energetics. Based upon our measured appearance energies, it appears that the pathway depicted in red is operational. Photoionization occurs upon vertical excitation from the structure Ia, where one acetaldehyde is strongly bound to water (bond distance 1.88 Å), and the weaker bond is much further (2.81 Å).

The calculated ionization energy of 9.61 eV matches the experimental IE of 9.78 eV well. Ionization from the structure IIIa is not operable since we do not observe any of the unprotonated structured depicted in IIIb. In case IIb, the proton is transferring from a formyl group to another acetaldehyde cluster, similar to that occurring in pure acetaldehyde clusters. However, the aforementioned proton transfer from an original Ia, upon photoionization is the most interesting one and explains the formation of protonated acetaldehyde-water clusters. Here water is essentially acting as a relay in transferring the proton from one acetaldehyde to another (Ib), reminiscent of a Grotthuss mechanism, where rapid exchange between a covalent and hydrogen bond takes place. A similar mechanism is also operable in the case of transfer in the trimer and tetramer acetaldehyde-water clusters based upon the experimentally measured appearance energies and calculated energies for the water-mediated relay-type mechanism. While we and others have used VUV photoionization coupled with electronic structure methods to probe proton transfer in clusters, we note that Farnik's group have used electron impact ionization, or sodium doped ionization as methods too. Very recently, they showed that proton transfer from pinene led to protonated water clusters larger than 7, and this was due to the proton's solvation energy,[89] while pyruvic acid can act as donor or acceptor of both protons and hydrogen from water clusters.[90]

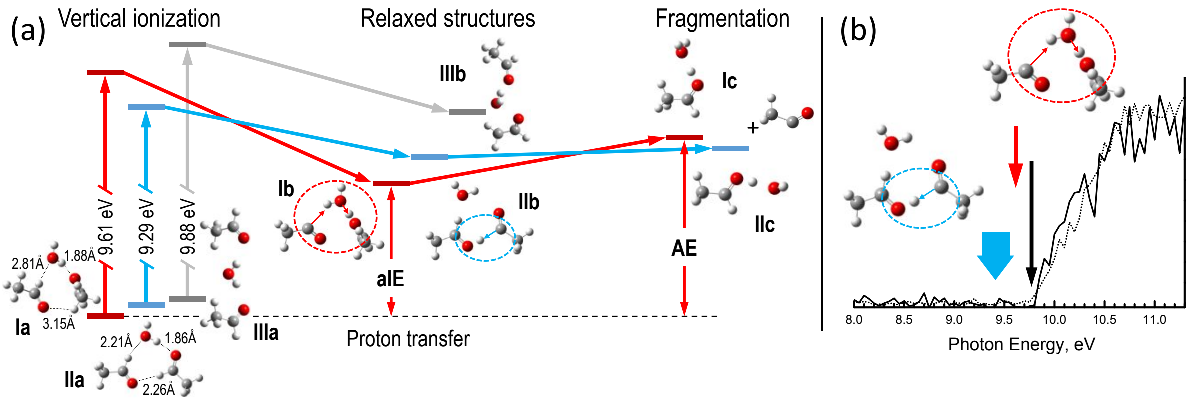

Fig. 12. (a) Schematic energy diagram for the ionization and fragmentation of three different isomers of acetaldehyde dimer–water complexes. The adiabatic ionization energy (aIE) and appearance energy (AE) is shown only for structure I. (b) Photoionization efficiency curve for protonated acetaldehyde-water cation. The blue arrow shows the calculated appearance energy for "conventional proton transfer" also marked with a blue circle in the figure, the red arrow shows the calculated "water mediated" proton transfer pathway marked with a red circle in the figure, the black arrow shows the experimental onset. Adapted from ref. 88 with permission from the PCCP Owner Societies.

Solvation and reactivity in ionized naphthalene–water clusters

Naphthalene is moderately hydrophobic and is one of the simplest polycyclic aromatic hydrocarbons (PAHs). PAHs may comprise up to 20% of the carbon budget in our galaxy and most PAHs condense onto the water-rich icy grain mantles. The photo-processing of water ice mantles containing PAHs by UV light has been studied and many complex organic species are generated, such as quinones and ethers.[91] Benzene-water cluster systems have been used as prototypical models for the understanding of the interactions of PAHs with water in ice mantles. Several characteristic features for the interaction of benzene with multiple water molecules have been established using molecular beams and spectroscopy: (1) water molecules tend to form a hydrogen bonded sub-cluster above the benzene ring with a weak π-hydrogen bond; (2) the ionization of the clusters results in a significant structural change and (3) large water clusters $(H_2O)_n$ (n > 3) leads to dehydrogenation of the benzene cation.[57, 92-97] While most studies of this kind have been carried out by employing benzene as a model for PAHs, and there have been recent vibrational studies on PAH water interactions,[98-100] there has not been a direct measurement of naphthalene-water photoionization in the gas phase to benchmark against theory and confirm early experimental measurements performed on PAH-water ices.[101, 102] In addition, the study of naphthalene-water can also shed light on the understanding of water-graphite and water-graphene interactions,[103] which can provide a molecular picture of water confinement in carbon nanotubes and graphene sheets.[104]

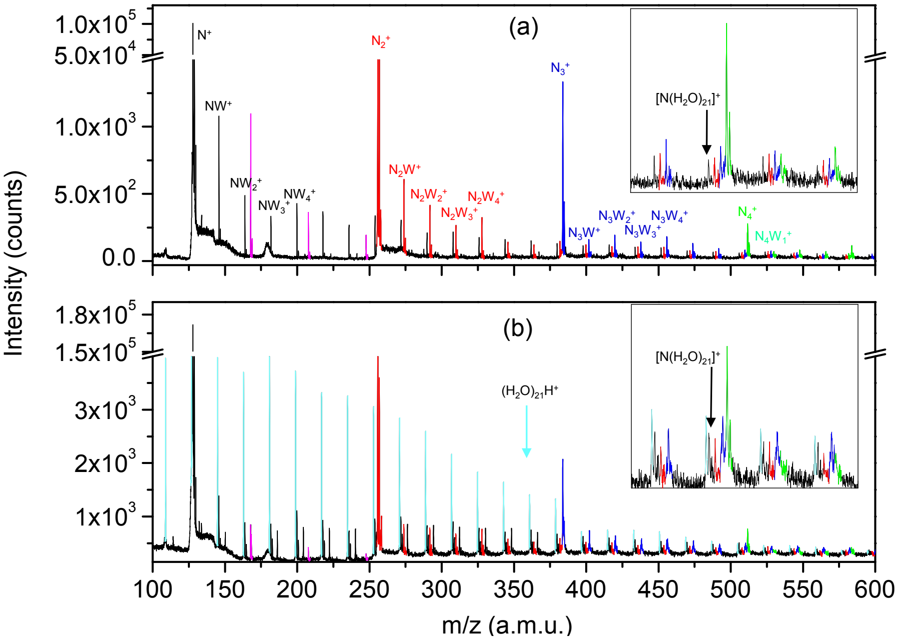

Fig. 13. Time-of-flight mass spectra of naphthalene-water clusters at (a) 10 eV and (b) 12.5 eV. $N_xW_y^+$ denotes $[\text{Naphthalene}_x(H_2O)_y]^+$. The inset shows the region at m/z 520 corresponding to $[N(H_2O)_{20\text{-}24}]^+$. The cyan arrow indicates $(H_2O)_{21}H^+$ while the black arrows indicate $[N(H_2O)_{21}]^+$. Reproduced from ref. 105 with permission from The Royal Society of Chemistry

We implemented our combined photoionization mass spectrometry methods together with theoretical calculations from Martin Head-Gordon to decipher the resulting dynamics in naphthalene-water clusters.[105] Our study shows different channels of ionization of the naphthalene-water clusters depending on energy of the ionizing photon. This is revealed in the mass spectra shown in figure 13, at two different photon energies. At 10 eV, only naphthalene and its clusters can ionize, while above 11 eV, water clusters begin to ionize. The appearance energies of these ions, revealed via PIE measurements, coupled with ionization energy calculations from different neutral geometries reveal the origin of the isomers present in the beam. A theme that appears from the results is that water tends to cluster above the π cloud of the naphthalene and typically do not interact with the side edges, and the photoionization dynamics of the mixed system is very similar to pure water cluster ionization above their ionization energies (<10.9 eV).

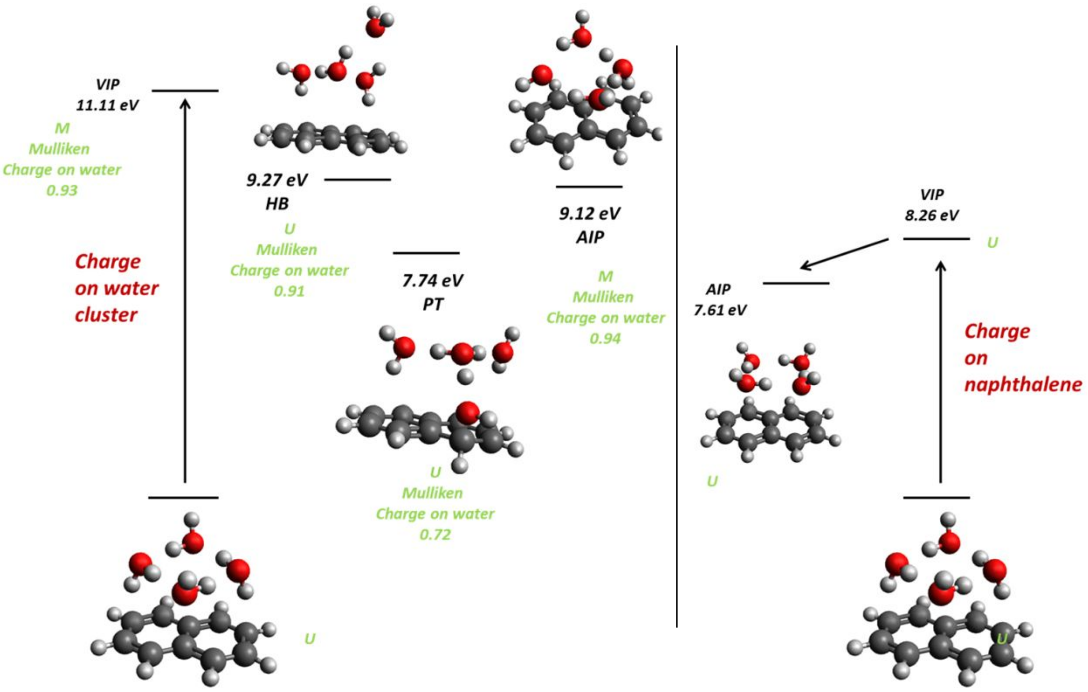

Fig. 14. Left: ionization of the water sub cluster. Right: Channels upon ionization of the naphthalene part of the cluster. Reproduced from ref. 105 with permission from The Royal Society of Chemistry.

Here we use Figure 14 to summarize the results for the case of four water molecules, the largest studied system to explain how ionization from either naphthalene or the water sub-cluster leads to different dynamics. The vertical ionization energy when naphthalene is being ionized is calculated to be 8.26 eV, agreeing well with an experimental appearance energy of 8.2 eV. When the photon energy is below the water ionization threshold, the naphthalene moiety of the cluster is ionized and no protonated naphthalene-water clusters are observed. Rearrangements of the water sub-cluster upon ionization enhance their charge dipole interactions and other induced interactions with cationic naphthalene while maintaining the hydrogen bonding network. In the case for the water sub-cluster ionization, the calculated vertical ionization energy is 11.11 eV, this agrees well with the experimental appearance energy of protonated naphthalene-water clusters at around 11 eV. When ionization occurs above the water ionization threshold, there is proton transfer within the water sub-cluster and hydroxyl radical emission. In addition, the generated hydroxyl radical can also react with naphthalene to form an adduct, and the proton is solvated by the other remaining waters. Based on the calculations and EDA, as we can see on the right of figure 14, water remains on top of the aromatic ring, and since naphthalene is carrying a charge upon ionization, the water molecules flip with the oxygen pointing towards naphthalene. This leads to favorable charge-dipole interactions, as well as polarization and some charge transfer between oxygen and naphthalene. In contrast, when ionization occurs from water, there is no flipping of the oxygen, and the structures are very similar to pure ionized water clusters. It is very interesting to see that that 'hemi-bond' and proton transfer type structures that have been postulated as transients in pure water cluster ionization are also present in naphthalene-water clusters, as shown in figure 14. These species should be observable spectroscopically, since recently Xie et al., using VUV photoionization in combination with IR spectroscopy, observed hemi-bonded structures in H_2S clusters[106] and for $(CH_3SH)_2^+$ bonded with H_2O, $(CH_3)_2CO$, CH_3SH and NH_3.[107] Coincidence spectroscopy where mass selected photoelectron spectra can be obtained could also be applied to these PAH water clusters, as recently demonstrated for pure PAH[108] and water clusters[109] at the French synchrotron SOLEIL.

As described in the work here, the ionization of larger clusters similarly undergo rapid proton transfer and fragmentation to produce protonated water clusters of the form $H^+(H_2O)_n$.

$$(H_2O)_n + h\nu \rightarrow (H_2O)_n^+ + e^- \rightarrow H^+(H_2O)_{n-1} + OH + e^- \qquad (1)$$

Reaction (1) produces protonated clusters regardless of the ionization conditions (photoionization or electron ionization) and clustering with various moieties. Energy selective fragmentation upon photoionization of water[110] and mixed clusters[44, 75] is the half-collision analogue of ion-molecule reactions of water cluster ions studied decades ago in flow reactors and collision cells[111, 112] coupled to mass spectrometry and more recently in an electric field.[113]

$$H_2O^+ + H_2O \rightarrow H_3O^+ + OH \qquad (2)$$

The molecular mechanism of water evaporation[114] is still not well understood and these kinds of collision studies can go some way in shedding light to this very fundamental process. For instance recent innovative experiments used collisions of water cluster ions with an argon beam, to measure energy distributions and subsequent evaporation dynamics.[115] The timescales of reaction (2) was only recently clocked with femtosecond X-ray spectroscopy[116] at an FEL in which the proton transfer between the water cation and neutral water leading to the elimination of the hydroxyl radical and formation of protonated water was mapped out in liquid water.

A future direction would be to use photoionization as a method to extract thermodynamic parameters in larger clusters with methods described here. Indeed, we have measured ion-induced growth of water clusters in a supersonic expansion as described earlier for methanol[24] and acetylene clusters.[54] The mass spectra shows non equilibrium distributions dependent on the distance between the nozzle and ionization source, analysis of which should allow access to kinetics and thermodynamics of these processes. Modelling the fluid dynamics of the supersonic expansion will be crucial for such an enterprise.[24] We plan to embed larger PAHs into water clusters to truly mimic astrochemical icy surfaces, measure evaporation rates, and perhaps also explore water confinement within these hydrocarbons. As the number of rings increase, PAHs begin to show curvature,[21] and it should be possible to generate such mixed clusters in our experimental apparatus. Another approach would be to sample PAHs from atmospheric flames, and collide such ions with water in a tandem mass spectrometer. Recently in collaboration with Nils Hansen from Sandia National Laboratory, we showed that we could generate alkylated single-core aromatic compounds and the fragment ions that correspond to the loss of saturated and unsaturated units containing up to a total of six carbon atoms.[117] Furthermore, the aromatic structures that form the foundational building blocks of the larger PAHs were identified to be smaller single-ring and peri-condensed aromatic species with repetitive structural features. For certain PAHs, water clusters were observed to be bound to the core, the water being present in the collision gas cell. This method will provide a rich source for interrogation with IR hole burning spectroscopy, where one could tune through the mass range to select any size of PAHs.

Exciton energy transfer in argon-water clusters

Water clusters coupled with photoionization can provide insight into a myriad of processes which are relevant to energy transfer and the study of excited states.[70, 109, 118] One such process is Penning ionization, in which an electronically excited atom transfers its energy to an adjacent second system, that subsequently ionizes, which has allowed for elucidation of dynamics in a number of systems. Similar processes were also observed in weakly bound complexes and clusters with the advent of ion momentum spectroscopy, leading to a revolution in the field of interatomic coulombic decay.[119, 120] It has been known since the 80's that pure rare-gas clusters can lead to exciton formation with their properties explored explicitly,[121] and that composite rare-gas complexes can generate processes reminiscent of Penning ionization.[122] The appeal of using these systems is that a molecular level picture of energy transfer and ionization could be followed from small clusters all the way to the continuum. Our search for non-fragmented water clusters led us in the direction of using Penning ionization as literature had suggested that under very cold conditions, such non-fragmented clusters, or hydroxyl retained within the cluster can be generated. When we applied the same procedure, very large backing pressure (7 bar) and small nozzle size (50 microns), we did observe both non-fragmented and fragmented water clusters. From a PIE analysis, we showed that the excitation process involved the transfer of the energy from an exciton formed in the solvating shell of argon around the water clusters to the embedded water cluster.[123] This leads to fragmentation while the evaporating argon atoms remove the excess internal energy, beyond the ionization energy in the water cluster, leaving a very cold cluster cation. Here the argon exciton is acting as an antenna to receive the VUV photon, and allowing ionization of a moiety with a lower ionization energy (schematically depicted in Fig. 15). Similar mechanisms have been invoked upon electron impact ionization of argon coated water clusters.[124]

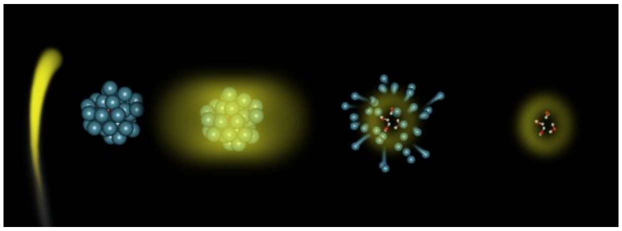

Fig. 15. Cartoon depicting exciton charge transfer (from left to right). VUV photon, Ar-water cluster, exciton generated in Ar shell and charge transfer occurs to water cluster, Ar atoms evaporate and remove excess energy, non-protonated water cluster ions remain.

This method is a way to probe excited states in both the host and guest clusters, and recently we have used it to probe the excited states of argon clusters in mixed acetylene-argon clusters. The vibrational levels of acetylene in the ground state are resonant with the Ar 4*s* energy levels, allowing for very efficient energy transfer; indeed these mixtures are used for making lamps. Furthermore, the binding energy of Ar-C_2H_2 is lower than that of Ar-H_2O, allowing us to resolve the spectra of Ar_n ($n = 1 - 7$). Finally, we note, that this method could be used to probe the long sought after excited states of water clusters,[125, 126] by generating clusters of water with a moiety of lower ionization energy, and most important, lower absorption cross section. We attempted this with PAH-water clusters since the IE of naphthalene is lower than that of water clusters. However, the large absorption cross section for naphthalene compared to that of water in the VUV region of interest stymied our efforts. We believe that with the advent of tunable VUV lasers on the ultrafast time scales, it should be possible to capture these elusive excited states.

The role of water in the photoionization of arginine in the gas and nano phase

We end this section on the use of mass spectrometry to probe electronic structure and reactivity in non-covalently bound systems with a study of the solvation of an amino acid – arginine. Arginine has multiple protonation sites that allows it to form different hydrogen-bond patterns that allows important biological functions,[127] for instance in sensing membrane potentials.[128] In solution, arginine has played a key role in driving crystallization of proteins, via its ability to form pre-nucleation clusters dependent on pH of the solution.[129] Therefore, an understanding of its ionization energy, both in the gas phase (to be tractable by ab initio theory) and in solution (to be relevant in chemistry and biology) is important. We have been interested in this molecule for more than two decades and only recently answered the question – what is the experimentally determined ionization energy of arginine?[130]

Using our gas phase molecular beam methods to generate an intact arginine molecule for clustering with water or alone proved unsuccessful, we never saw an intact molecular ion. We then implemented a method of impacting intense focused particle beams, generated by aerosol methods, on a heater, which gives rise to gas phase species. Subsequent ionization via VUV radiation generates fragment-free mass spectra, and we have studied a number of amino acids and peptides with this method.[27] To our surprise, we found that arginine fragmented extensively, and only miniscule amounts of the parent ion was measured at pH =1 (Fig. 16a). However, we did manage to measure its appearance energy based on that ion. Then we turned to Anna Krylov, with whom we had a long collaboration on studying photoionization in water and microhydrated biomolecules to try and explain why arginine would fragment so readily in the gas phase. Arginine posed a problem for calculations, with its numerous isomers, over 100 in the gas phase alone. The large number of isomers arises due to the long and flexible side chain with the guanidine group, which can form various hydrogen bonds. Vertical ionization energies of the most abundant isomers were calculated using the EOM-IP-CCSD/MP method. To understand structural relaxation induced by ionization and subsequent fragmentation dynamics, geometry optimization of ionized arginine molecules and ab initio molecular dynamics calculations using density functional theory were used. The simulations showed that low yield of parent ions arise exclusively upon photoionization but not from thermal decomposition of the neutral isomers formed during evaporation of the aerosol. We note that the experimental onset of 8.05 ± 0.1 eV is the closest to the computed adiabatic IE of the canonical isomer (~7.7 eV) that did not dissociate. More abundant tautomeric forms and the zwitterionic isomer have a lower adiabatic IE of 7.5 eV (computed) and undergo dissociation in the simulations under ambient conditions. Thus, we do not expect these forms to contribute to the m/z 174 photoionization signal. Consequently, we assign the experimental photoionization onset of 8.05 ± 0.10 eV to the ionization of the canonical isomer.

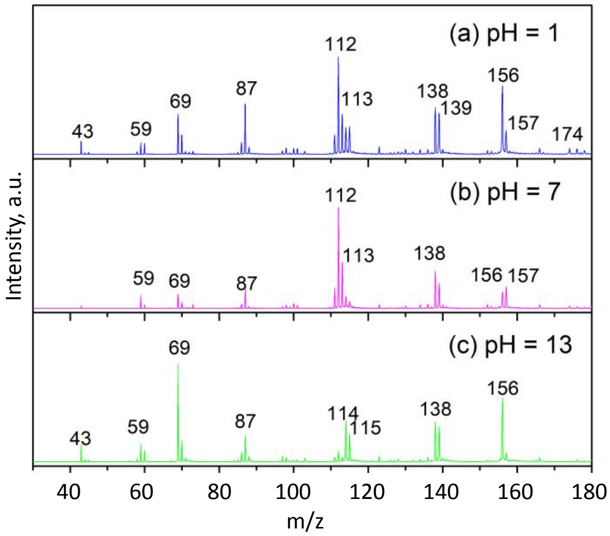

Fig. 16. Mass spectra of gas phase arginine generated from solutions at pH 1, 7, and 13, respectively, measured at 9 eV. The parent ion of arginine is only seen at pH=1 at m/z 174. Reprinted with permission from ref 130. Copyright (2019) American Chemical Society.

The same aqueous aerosol approach that allowed us to generate gas phase arginine was then introduced into a velocity map imaging photoelectron spectrometer to generate valence band photoelectron spectra to understand how solvation affects the ionization properties of arginine (figure 17). This was inspired by experiments performed by Chia Wang in Taiwan, who used aerosol based VUV photoelectron spectroscopy to follow proton transfer as pH was varied on biological aerosols.[131, 132] We had employed VUV photoelectron imaging spectroscopy in 2005 to probe glycine and phenylalanine-glycine-glycine nanoparticles[30] and recently arginine using soft X-rays,[133] which will be discussed later in the article. To understand the pH dependent shifts in the valence photoelectron spectra (Fig. 17) we again turned to theory. To model ionization in aqueous solution, calculations with implicit and explicit solvent models were carried out. The solvent has a strong effect on the relative energies of the isomers, strongly stabilizing the zwitterionic isomers, with a difference of 0.3−0.5 eV relative to the canonical and tautomeric forms. Furthermore, upon ionization, calculations show that the structures are stable in contrast to the gas phase, suggesting that the solvent has a strong stabilizing influence on the system. Depending on the acidity of the solvent, the population of isomers changes, and this is clearly reflected by the spectra obtained at various pH values. We expect that the *p* conformer is prevalent near physiological conditions, whereas the *z* form becomes dominant in basic solutions. The experimental spectra show an overall red shift as the pH increases. However, the interpretation of the spectra and the comparison between the experimental and theoretical results are difficult due to the spectral overlap of valence ionization of water and arginine, yet the calculations show the red shift between *z* and *p* isomers, in qualitative agreement with the experiment.[130]

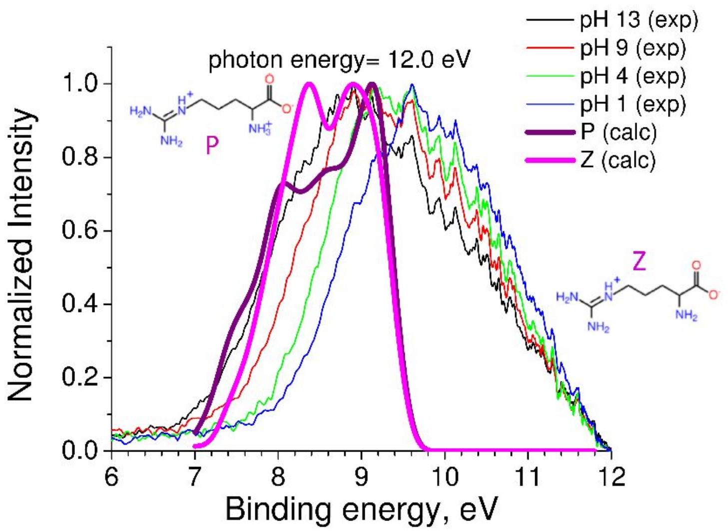

Fig. 17. Experimental photoelectron spectra of aqueous arginine aerosols at various pH values measured at a photon energy of 12 eV and calculated spectra of protonated and zwitterionic forms of arginine. Only vertical IEs below 9.5 eV were considered for these spectra due to overlap of water ionization around 10 eV. Adapted with permission from ref. 130. Copyright (2019) American Chemical Society.

Soft X-ray velocity map imaging of nanoparticles

Continuing on the theme of probing nanoparticles, we now focus on applying soft X-rays to the problem. In contrast to VUV photons, which probe the valence level of molecules, X-rays can access core levels and report on the local electronic structure of the system. Recent review articles on the application of these methods to aqueous system, particularly in liquid jets provides the framework of the available spectroscopies.[134-136] Here we will use these methods to probe reactivity in aerosol chemistry, obtain phase information on aqueous nanoparticles and discuss a very recent method of obtaining electron scattering cross-sections from condensed matter. In contrast to liquid microjets and microdroplets typically used to probe aqueous and liquid environments,[135] we chose to couple aqueous nanoparticles with our VMI photoelectron spectrometer. The VMI technique has an advantage of collecting full 4π distribution of emitted electrons in comparison to limited collection angle of hemispherical analyzers, mostly used in soft X-ray photoelectron spectroscopy (XPS). Application of aerosols instead of static samples also has advantages, such as probing fresh aerosol surface by every X-ray photon eliminating problems such as X-ray sample damage as well as surface charging.

We illustrate the power of VMI as applied to gas phase molecules and nanoparticles with both VUV and soft X-rays in figure 18. The raw VMI spectra of xenon, collected at different photon energies are presented in Fig. 18a and 18b. Both spectra possess some similarity, demonstrating double rings corresponding to different spectral features of xenon: to the Xe 5p and 4d lines (Fig. 18a and 18b, correspondingly). To obtain a photoelectron spectrum from the VMI image, a reconstruction, analogous to the Abel transform, is needed. The photoelectron spectrum reconstructed from the image shown in Fig. 18b using pBASEX algorithm is presented in Fig. 18c. The spectrum has two sharp peaks corresponding to the Xe 4d doublet as well as broader peaks, assigned as Auger NOO peak at kinetic energy (KE) of 30 eV and a peak due to double Auger decay of 4d holes at KE of ~2 eV. The VMI spectra of squalene nanoparticles collected at photon energy of 15 and 315 eV are shown in Fig. 18d and 18e, respectively. The spectrum, collected using VUV radiation is more intense from one side. The shallow penetration depth of VUV radiation in the nanoparticle leads to preferential emission of electrons from the NP side, exposed to the light, as observed in Fig. 18d. In contrast, the soft X-ray radiation is almost not attenuated in the NP and causes a symmetrical distribution of the emitted electrons in the bright part of the image (Fig. 18e). The photoelectron spectrum reconstructed from the latter VMI spectrum (Fig. 18f) similar to the one presented in Fig. 18c, contains a sharp peak, corresponding to emission of the C 1s core photoelectrons. Apart from the C 1s peak, the spectrum possesses a broad distribution of low KE secondary electrons peaking at KE ~3eV. The secondary electrons appear due to numerous inelastic collisions of either photo- or Auger electrons, leading to the broad, structureless distribution of low KE electrons. In addition, the original VMI images contain information on angular distribution of emitted photoelectrons (clearly visible in Fig. 18a and 18e).[31] While the secondary electron angular distribution is completely symmetric, there is angular anisotropy in the core level photoelectrons (figure 18e) and this is discussed later.

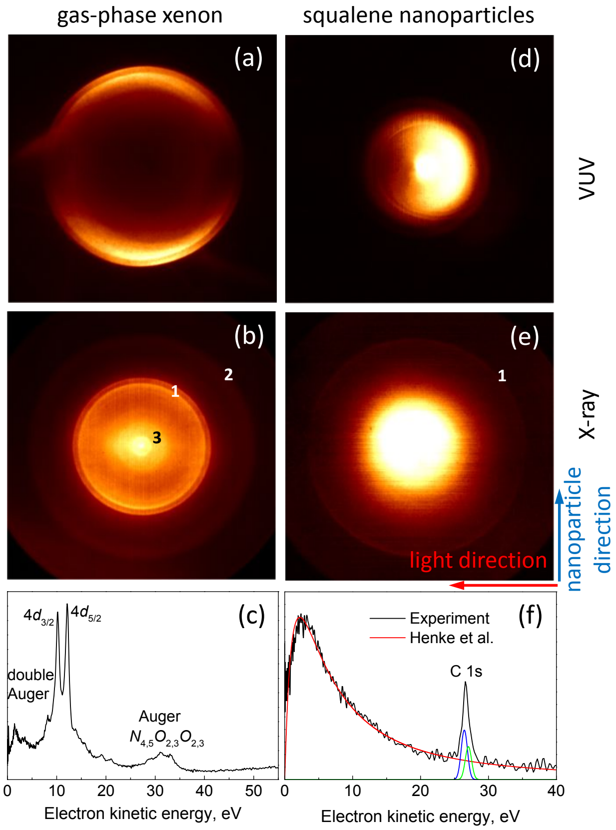

Fig. 18. Velocity map images of gas phase and nanoparticle samples: (a) and (b) VMI spectra of xenon collected at photon energy of 22 and 80 eV, respectively. (c) Spectrum of xenon reconstructed from (b). (d) and (e) VMI spectra of squalene nanoparticles, collected at 15 and 315 eV. (f) Spectrum of squalene nanoparticles, reconstructed from (e). Adapted with permission from ref. 31. Copyright (2017) American Institute of Physics.

Inelastic and elastic low energy electron scattering in nanoparticles

Electron transport in condensed matter is a fundamental problem in physics and has applications in radiation biology,[137] astrochemistry,[138] and material science.[139] Furthermore, electron interactions with condensed matter has allowed electron microscopies, X-ray photoelectron spectroscopy, and electron energy loss spectroscopy to become exquisite tools to probe physical, chemical, and biological processes on the nanoscale. While for electrons with KE > 50 eV, interactions in the condensed phase is well understood, there is a paucity of information, both experimental and theoretical at lower energies. Just from the point of radiation biology, low energy electrons and their interactions with water and biological molecules can give rise to myriad chemical processes which are not very well understood, for instance the hydrated electron's vertical detachment energy,[140, 141] hence both VUV and soft X-ray spectroscopy were used to shed light on these problems.[137]

Soft X-ray spectroscopy is a surface sensitive technique, where the probing depth is limited by the finite electron inelastic mean free path (IMFP). The concept of "universal curve" was adopted in the early days of photoelectron spectroscopy.[142] According to the concept, most of materials demonstrate similar trend of IMFP at different electron KE (the curve is shown in Fig. 19a). In the high KE regime (KE > 100 eV), the IMFP of different materials are similar and increase with KE. Since its inception, it was demonstrated that for KE < 50 eV, the IMFP is material dependent and may significantly deviate from the "universal curve".[143] We applied our VMI photoelectron spectroscopy approach to investigate the sampling depth of low KE electrons. Initially we tested the feasibility of the measurement, using a classical overlayer approach, where electrons, emitted from a substrate are attenuated by layers of the studied material. Size selected nanoparticles of KI were coated by layers of squalene. VUV radiation caused emission of valence electrons from KI, the intensity of which was attenuated by squalene layers of known thickness. The experiment allowed for determination of the electron attenuation length (EAL) for very low KE electrons (KE = 1.1 – 4.4 eV).[144] It was found that with KE increase, the EAL decreases from 15.6 to 3.3 nm, following the "universal curve" trend. The experiment was limited to small electron KE range, dictated by choice of the core-shell system.

However, soft X-ray photoelectron spectroscopy with VMI contains sufficient information to extract the relative IMFP values.[145] The low KE secondary electron signal, observed in a center of VMI images, provides information identical to the total electron yield near edge X-ray absorption fine structure (NEXAFS) spectroscopy. Intensity of that signal is proportional to the photoabsorption cross-section σ(KE) of the nanoparticle, whereas the intensity of the photoelectron peak is proportional to the product of σ(KE) and the IMFP. Hence, combining the intensities of photo- and secondary electrons, the relative IMFP can be obtained. With this method, the absolute value of the squalene IMFP was obtained by normalization of the IMFP for KE = 50 eV to a published value. The obtained IMFP KE dependence also follows the "universal curve" trend (Fig. 19a). Moreover, it correlates with the EAL values obtained by us for an analogous hydrocarbon squalane using the aforementioned overlayer method combined with VUV photoemission, although strictly speaking, the IMFP cannot be directly compared to the EAL.

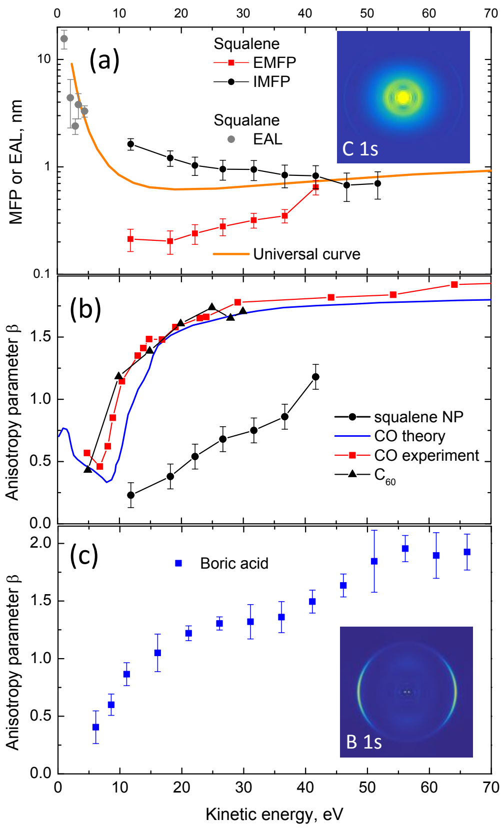

Fig. 19. (a) IMFP and EMFP for squalene compared to low KE EAL for squalane. (b) Anisotropy parameter β for squalene nanoparticles compared to β parameter of gas phase CO and C_{60} molecules. (c) Anisotropy parameter β for dry boric acid nanoparticles. Inserts in (a) and (c) represent reconstructed VMI spectra of squalene at 315 eV and boric acid at 215 eV, respectively, demonstrating anisotropy of photoemission of 1s electrons. (a) and (b) Adapted with permission from ref. 145. Copyright (2019) American Institute of Physics.

The angular distribution of the photoelectrons emanating from nanoparticles is dependent on the incident photon energy and resulting kinetic energy of the photoelectron. Similar observations have been made in the literature in experiments on silica nanoparticles[146] and liquid water jets.[143, 147] Typically photoemission of the C 1s electron from gas phase atoms should result in an outgoing p-wave electron, angular distribution of which can be characterized with a β parameter.[148] However, condensation of atoms or molecules into a solid complicates the photoemission process. In solids, the photoelectrons need to travel some distance before they could escape through the surface. During this travel, elastic collisions will change the initial angular distribution of photoelectrons. The degree of the change depends on the number of encountered elastic collisions and is clearly visible in Fig. 19b, where β parameter for gas phase CO and C_{60} is compared to β parameter of photoelectrons, detected from condensed squalene nanoparticles. We used Monte Carlo simulations to model the transport of the photoelectrons in solid, where all input parameters were experimentally determined parameters (such as IMFP, β parameter, etc.). The simulations provided values of the elastic mean free path (EMFP), an important parameter for understanding low KE electron transport (Fig. 19a). It was found that 12 eV photoelectrons on average experience 8 elastic collisions, which significantly change the electrons trajectories. The high number of elastic collisions for low KE electrons demands particular attention when using low KE photoelectrons for depth profiling. Indeed, the knowledge of IMFP alone is insufficient for that and requires consideration of both IMFP and EMFP for understanding from what depth the detected low KE electron may originate. A similar rise of β parameter with increase of photoelectron KE we observed for B 1s photoelectrons emitted by dry nanoparticles of boric acid (Fig. 19c). The rise of β parameter is steeper than observed for C 1s photoelectrons emitted from squalene and lies in between of β parameters for C 1s collected from gas phase molecules and condensed hydrocarbon, represented by squalene nanoparticles. The steeper rise of β may suggest that elastic scattering is less efficient in boric acid than in squalene. However, the β parameter KE dependence measured here for squalene at the carbon K edge using VMI is exactly the same as that measured in a water liquid jet with a hemispherical photoelectron spectrometer at the oxygen K edge.[143] This could be due to chemical structure or phase (amorphous, glassy or crystalline) and in future experiments, by judiciously changing conditions of nanoparticle formation coupled with exciting various atomic transitions should shed light on this intriguing observation. Another approach would be to probe the anisotropy in angular distributions in mixed nanoparticles – for instance in glycerol water mixtures. By varying the molar content of each constituent, nanoparticles can be formed in various phase states, as the hydrogen bonding network is disrupted. Furthermore, there could be layering between glycerol and water leading to different length scales for electron scattering. Theory can also provide insight into these problems by calculating photoelectron angular distributions emanating from different orbitals and taking into account the effects of electron scattering. Recent theoretical work from the Krylov group, where Dyson orbitals formalism was used to calculate X-ray photoelectron spectra of ground state of adenine and excited states of uracil are encouraging in this respect.[149]

Solvation and phase changes in aqueous nanoparticles

We used the VMI-NEXAFS technique to probe nanoparticles composed of pure water and water – NaI solution to study solvation and phase changes in aqueous systems.[31] The NEXAFS spectrum of pure water (Fig. 20a) contains characteristic features, previously observed in liquid jet experiments.[150] These features, named pre-, main-, and post-edge features are explained by different coordination of the H-bonding network. While we observed similarity with the liquid jet NEXAFS spectra,[150] there was a distinction in relative intensity of the pre- and post-edge features. This was explained by coexistence in the probing region of 40% liquid and 60% frozen water nanoparticles, and is a result of evaporative cooling of the particles. Addition of small amount of NaI (0.038M) to the solution led to change of the NEXAFS spectrum intensities of pre- and post-edge features in comparison to pure water spectrum (Fig. 20b). This small concentration of NaI cannot cause such a strong effect as to perturb the tetrahedral coordination of water molecules. We explained the observation by a propensity of iodide anions for the interface.[151] Higher concentration of iodide anions leading to perturbation of water molecule coordination, coupled to enhanced surface-to-volume ratio in aqueous nanodroplets, as well as small probing depth led to the observed strong change of the spectrum, caused by small concentration of NaI.[31] By carefully adjusting the nanoparticle and X-ray beams we could measure the NEXAFS spectrum of gas-phase water molecules (Fig. 20c), evaporating from the surface of water nanoparticles. A future effort would be to install a physical chopper between the nanoparticle beam and X-ray radiation, to allow the measurement of neutral time of flight of the evaporating gas phase molecules. This could then be applied to probe the dynamics of water and other aqueous systems as demonstrated so effectively by Nathason.[152]

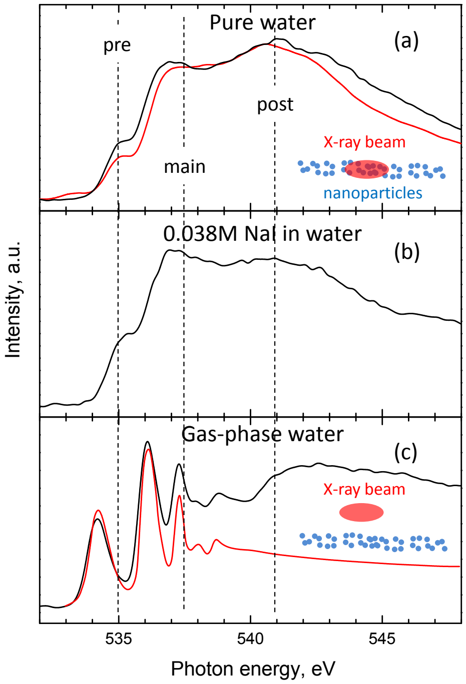

Fig. 20. NEXAFS oxygen K edge spectra of (a) pure water nanodroplets. Experimental data, shown by black line are compared to a linear composition of 40% liquid water and 60% ice.[150] (b) Nanodroplets of water – NaI solution. (c) Gas phase water NEXAFS spectrum, obtained by sampling signal above water nanoparticle beam (see insert) compared to literature spectrum of gas-phase water.[150] Adapted with permission from ref. 31. Copyright (2017) American Institute of Physics.

pH dependent proton transfer in arginine nanoparticles

The capability of VMI-XPS to probe charge states in aqueous systems is focussed on the amino acid – arginine, [133] its importance described earlier.[130, 133] Arginine also plays a role in nucleation and subsequent crystallization which is at the heart of various scientific disciplines, but still the understanding of the molecular mechanisms underlying phase separation and the formation of the first solid particles in aqueous solution is rather limited.[153] This has enormous ramifications for the self-assembly of natural or synthetic amphiphiles to build well-defined nanostructures with controllable function at the molecular level driven by non-covalent interactions. Arginine has a flexible molecular structure, composed of a guanidinium head group and an alpha amino acid tail held together by an aliphatic hydrocarbon backbone. The protonation of the guanidinium group and the deprotonation of the carboxyl group leads to a zwitterionic structure. Coupled with the unique properties of the planar guanidinium group, allows for inter- and intramolecular interactions (hydrogen bonding, ionic interactions) which leads to very interesting solvation, nucleation and crystallization dynamics. This alteration in the strength of hydrophobic interactions allows for a strategy to tune it to optimize molecular recognition and self-assembly processes,[154] act as a glue for modulation of biomolecular function,[155] and finds application in methods for cell penetration and drug delivery.[156] These interactions depend subtly on the very high acid dissociation constant (pKa) which is typically posited to be around12.5. Nevertheless, there is evidence in the literature that the actual pKa value can be even higher than 12.5. Aqueous aerosols from arginine solutions at pH of 1, 7, and 13 were probed at C and N 1s levels.[133] The arginine molecule contains six carbon atoms in four different chemical environments and four nitrogen atoms in two environments, significantly complicating analysis of the resulting XPS spectra. To ameliorate this, we applied a "building block" approach, separating the molecule into glycine and guanidine moieties. Their aqueous solutions at similar pH were studied using the same technique and the obtained XPS peak assignment was used to decipher the spectra of arginine. Shown in Fig. 21, are carbon atoms in different chemical environments labeled with different colors: one C atom in a protonated guanidinium group (red color), one C atom in a carboxyl group (blue color), two C–C atoms (black color), and two C–N atoms (green color). The analysis of the spectra revealed that similarly to glycine, arginine's carboxyl group is deprotonated when pH is increased from 1 to 7. At pH 13, the amine group becomes deprotonated. But the most interesting observation is that the guanidinium group stays protonated even at the highest investigated pH = 13, confirming that the pKa of the guanidinium group in arginine is larger than 13. Future experiments seek to use these signatures of the location of the proton, coupled with a visualization of the hydrogen bond network by probing at the O edge to understand self-assembly and growth processes in amino-acid lipid solutions.

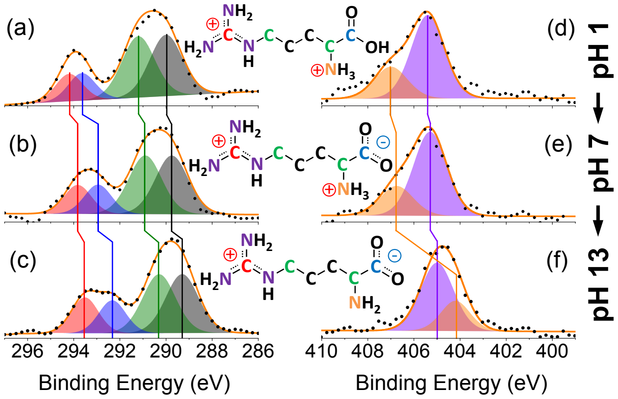

Fig. 21. XPS spectra of arginine in aqueous nanodroplets at different pH conditions, measured at C 1s (a-c) and N 1s (d-f) edges. Reproduced with permission from ref. 133 with permission from John Wiley and Sons, copyright 2017.

Exploring chemical reactivity in hydrocarbon nanoparticles

The physics and chemistry of aerosols in the atmosphere is complex, and a recent review by Bzdek and Reid[157] outlines scope of the problems that arise in studying such systems. The formation and nucleation of particles from gas phase precursors, physical and chemical processes on the particle surface and in the bulk span a range of temporal and spatial scales. Here at Berkeley, we have been interested in probing these processes with the tools of VUV photoionization mass spectrometry and photoelectron spectroscopy. In this perspective we provide snapshots of work ongoing in probing phase changes and chemistry in hydrocarbon aerosols. These aerosols can exist in different phase states: solid, liquid, and highly viscous, which can change the atmospheric fate of these particles.[158-161] In viscous, diffusion-limited aerosols, species at the aerosol surface are expected to react more rapidly than molecules residing in the nanoparticle interior, forming steep chemical gradients. Typical aerosol techniques applied to the probing entire particle volume, such as aerosol mass spectrometry or scanning electron microscopy, are not surface sensitive and cannot provide information on formation and dissipation of such chemical gradients. Surface sensitive techniques, such as soft X-ray photoelectron spectroscopy, are needed to study the surfaces of particles experiencing atmospheric reactions and this is described here.

Soft X-ray photoelectron spectroscopy was applied to investigate kinetics of the ozonolysis of squalene nanoparticles.[162] The X-ray photoelectron spectroscopy was able to resolve peaks at C 1s edge corresponding to differently bound carbon, such as: C=C, CH_x, C-O, and C=O bonds (Fig. 22a). The analysis of C=C peak decay with increase of ozone exposure yielded uptake coefficient for the decay of the double bonds in squalene. A similar coefficient was obtained from a NEXAFS measurement at C 1s (Fig. 22b) and O 1s edges. In this particular case, XPS, NEXAFS, and ultraviolet photoelectron spectroscopy measurements resulted in very close values of uptake coefficients despite the different probing depth of the methods. This is explained by the fact that squalene is liquid at room temperature; its oxidized nanoparticles can intermix, resulting in a homogeneous composition in the probing region of the VMI spectrometer.

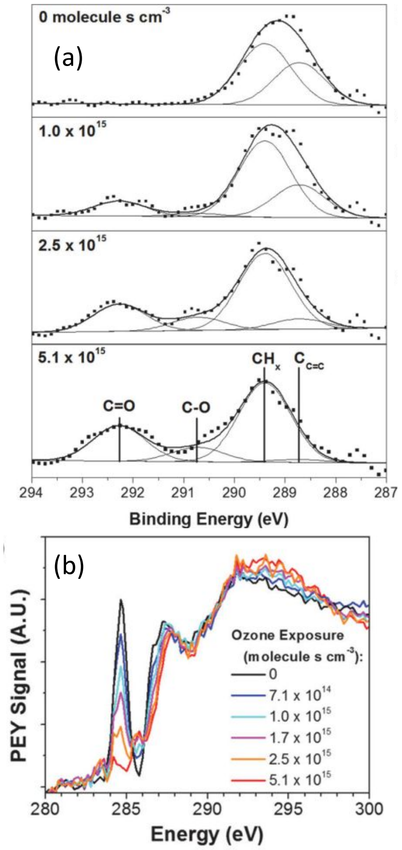

Fig. 22. (a) XPS spectra of squalene nanoparticles at different oxidation conditions. (b) NEXAFS spectra of carbon K edge of squalene nanoparticles at various ozone exposures. Reprinted with permission from ref. 162. Copyright (2016) American Chemical Society.

X-ray spectroscopy can be applied to study aerosol particles that exist in highly viscous, diffusion-limited states, and where steep chemical gradients are expected to form during photochemical processes. Under these conditions, species at the aerosol surface are more rapidly transformed than molecules residing in the particle interior. The heterogeneous reaction of hydroxyl radicals (OH) on ~200-nm particles of pure squalane (a branched, liquid hydrocarbon) and octacosane (a linear, solid hydrocarbon), and binary mixtures of the two are used to understand how diffusion limitations and phase separation impact particle reactivity.[163] Liquid at room temperature squalane ($C_{30}H_{62}$) and solid octacosane ($C_{28}H_{58}$) represent two opposite cases, where squalane molecules can diffuse in the aerosol particle, while octacosane molecules are immobilized and can therefore lead to steep chemical gradients on the surface of octacosane nanoparticles. Bulk sensitive aerosol mass spectrometry was used to extract the effective heterogeneous OH uptake coefficient and oxidation kinetics in the bulk. Whereas the chemical composition of the surface was probed by XPS of C 1s edge and NEXAFS of C 1s and O 1s edges (Fig. 23 bottom), both techniques resulting in comparable rate constants: (3.0 ± 0.9) × 10^{-13} and (8.6 ± 1.2) × 10^{-13} cm^3 $molecule^{-1}$ s^{-1} for squalene and octacosane particles, correspondingly. Higher rate constant for octacosane indicates that although the bulk composition of octacosane changes slower than that of squalene, due to its higher viscosity, the surface composition changes much more rapidly, creating a highly oxidized layer around an unoxidized nanoparticle core. This is shown schematically in figure 23 (top).

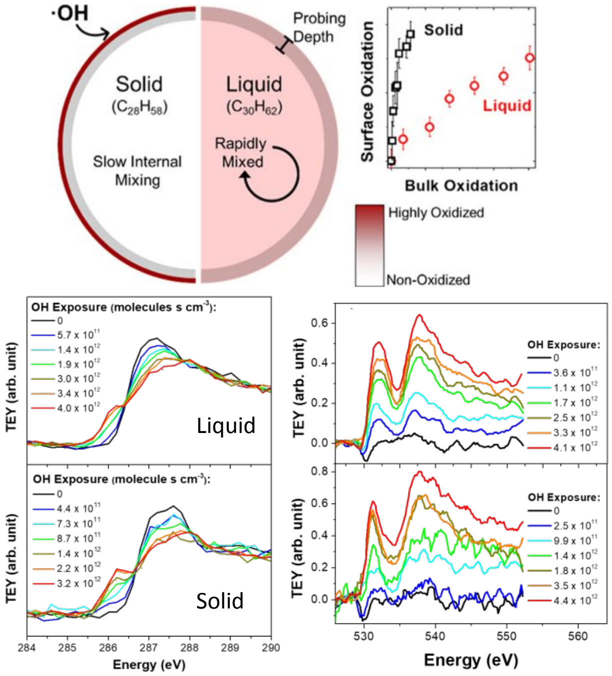

Fig. 23 Top: scheme of heterogeneous oxidation and formation of chemical gradients in nanoparticles of solid octacosane ($C_{28}H_{58}$) and liquid squalane ($C_{30}H_{62}$). Bottom: X-ray absorption spectra at carbon K edge (left) and oxygen K edge (right) of squalane and octacosane nanoparticles, collected at different OH exposures. Reprinted with permission from ref. 163. Copyright (2019) American Chemical Society.

Probing synthetic nanoparticles with X-ray spectroscopy

Below we describe how our approach of VMI based nanoparticle X-ray spectroscopy can be applied to probe the effect of confinement,[164] evaporation,[114] and phase changes particularly for water.[150] The studies described earlier used homogenous nucleation (squalene, squalane, and octacosane) or atomization of either pure water or aqueous solutions to generate nanoparticles. The atomized solutions can be studied as is, as was done for arginine in aqueous environment or water – NaI nanoparticles. Alternatively, solvent (water in this case) can be evaporated to generate dry nanoparticles of solute. This approach was used to make dry nanoparticles of boric acid for the results described earlier in figure 19c. Another approach is to start from synthesized nanoparticles dispersed in solvent and to use the atomizer to generate droplets of the solvent, containing nanoparticles. The solvent can be evaporated, using different approaches, leaving unsupported synthesized nanoparticles for interrogation with X-rays.

This approach is being applied to study water confinement in nanoporous silica using vibrational and X-ray spectroscopy.[165] We have recently developed a simple strategy of using Zn ion encapsulated dendrimers to build mesoporous silica nanoparticles of various internal hollow diameters ranging from 2-15 nm. The mesoporous shell itself consists of a porous network with nm dimensions. The internal void space allows for interrogating liquids in a confined space, and the huge surface area will allow for sensitive probing of solid-liquid interfacial chemistry. While X-ray photoelectron spectroscopy was used to obtain electronic structure information on colloidal silica nanoparticles using liquid jets,[166-168] and attosecond XUV streaking from aerosolized silica nanoparticles[169] have been reported in the literature, we propose to extend these studies to use electron angular information to provide a more complete picture on the evolution of water phase changes within the nanoparticle. Not only will we be able to determine the thickness of the shell of silica nanoparticles, we also anticipate that information on chemistry located within the environment of these nanoparticles will become accessible. It is as if we are using the interior of the particle as a container to observe phase changes as a function of internal volume. One can then judiciously tune the synthesis parameters to probe nucleation and material growth that has hitherto not been attempted with X-ray based spectroscopy.

To test if our methods can probe the interior of porous silica, nanoparticles containing copper ions surrounded by 5-10 nm silica shell were synthesized. Result of NEXAFS measurements at Cu L edge, shown in Fig. 24a, demonstrates that even in this case we can probe the interior of the nanoparticle. For comparison the spectrum, collected from 1 wt% aqueous $CuSO_4$ nanoparticles, is also shown in Fig. 24a. NEXAFS spectra of O 1s edge of synthesized solid and mesoporous silica nanoparticles are shown in Fig. 24b and 24c (acetonitrile was used as a solvent to eliminate any contribution from the oxygen edge). The spectra are compared to the literature spectra for quartz[170] and vitreous silica[171] and demonstrate a good correlation.

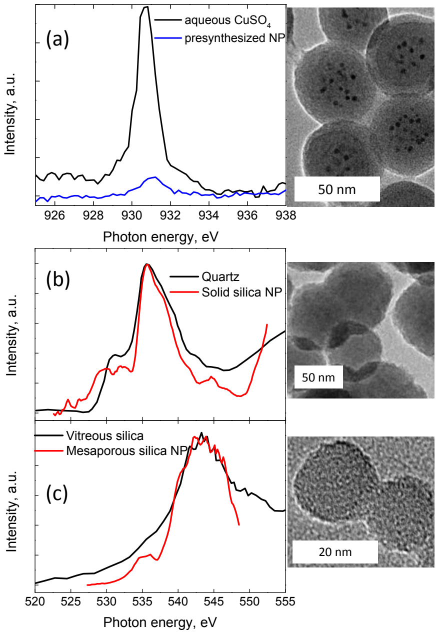

Fig. 24. NEXAFS spectra collected from synthesized nanoparticles together with TEM images of the nanoparticles. (a) Core-shell silica nanoparticles at Cu L edge, with core containing copper ions, coated by 5-10 nm silica shell. NEXAFS spectrum of aqueous $CuSO_4$ nanoparticles is shown for comparison. (b) Spectrum at oxygen K edge of solid silica NP compared to spectrum of quartz.[170] (c) Mesoporous silica NP spectrum compared to vitreous silica.[171]

Future

With the advent of free electron lasers and higher harmonic generation (HHG) in the VUV and soft X-ray regime, we take pause to think what kind of science described in this perspective can still be pursued at a 3rd generation synchrotron. The broad tunability across photon energies and average photon flux are two of the biggest advantages that synchrotron radiation can provide with relatively easy access. However, it is clear that the chemical physics and physical chemistry community that uses synchrotrons need to think creatively and innovate to remain at the cutting edge of science, and not follow the path of the atomic, molecular and optical sciences community who have migrated to FEL's and HHG sources. Recently fiber based lasers have been able to demonstrate synchrotron like quality in terms of power with isolated harmonics,[172] however tunability is still a concern. These sources are geared more towards angle resolved photoemission on solid systems, but can easily be applied to molecular and nanoparticle beams.[136]

We conclude our perspective with new science directions being pursued here at Berkeley Lab. Our modest efforts showcased here in the VUV region, coupled with innovations coming out of the Swiss Light Source[173] and Synchrotron SOLEIL[109] who are using coincidence methods to probe catalytic chemistry and cluster photoionization dynamics respectively can go some way in this new direction. A decade ago, we felt that pump-probe spectroscopies could be a future direction for probing VUV photoionization dynamics.[2] However, due to the mismatch of frequencies, synchrotrons typically work at MHz repetition rates, while lasers at that time and even now are hard pressed to provide sufficient photons at that rate to make good statistics for these demanding experiments. Progress has been made at 3rd generation synchrotrons,[174] and in figure 25, we show implementation of MHz laser systems to monitor light-induced picosecond electronic dynamics at the interface between N3 dye molecules and a nanostructured ZnO semiconductor substrate using time-resolved soft X-ray photoelectron spectroscopy at the ALS.[175] This method of pump-probe spectroscopy spearheaded by Oliver Gessner at Berkeley lab has now led to an understanding of the electronic and lattice contributions of CuO[176] with X-ray transient absorption and triplet excitons in metal-organic heterojunctions with X-Ray photoelectron spectroscopy.[177] Recently Smith and Saykally[135] reviewed the field of soft X-ray absorption spectroscopy of liquids and solutions, and it was interesting to note that there was not a single example of a two color experiment probing the excited state at a synchrotron. In contrast, a perspective on ultrafast photoelectron spectroscopy of aqueous liquids, showcases examples of pump-probe experiments of redox reactions and charge transfer to solvent reactions using lab based HHG liquid microjet methods.[136] Our nanoparticle source, coupled to VMI photoelectron spectroscopy could be implemented to follow excited state dynamics in nanoparticles, and charge transfer by embedding these nanoparticles in aqueous aerosols as demonstrated for CdSe nanocrystals[178] and quantum dots[179] using HHG sources. It should also be possible to couple graphene encapsulated cells,[180] microfluidic devices[25] and other reactors commonly used at the synchrotron into the interaction region of our VMI photoelectron spectrometer to enable the study of solvation and charge states in the excited state.

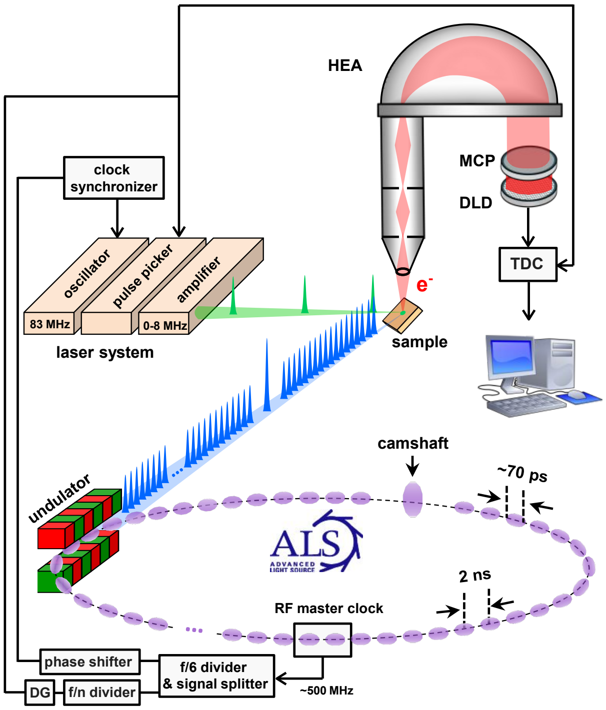

Fig. 25. Setup for picosecond time-resolved laser-pump/X-ray photoemission probe spectroscopy at the ALS. Key components of the electronic laser/X-ray synchronization scheme are indicated (DG – delay generator, HEA – hemispherical electron analyzer, MCP – microchannel plate, DLD – delay line detector, TDC – time-to-digital converter). Reproduced from ref. 175 with permission from The Royal Society of Chemistry.

The Advanced Light Source is over 25 years old now, as is the chemical dynamics beamline. A new initiative is to upgrade the ALS to a diffraction-limited storage ring (DLSR)[181] and have full transverse coherence in its light output, perhaps as early as 2026. The advent of DLSRs will provide new capabilities that bridge local and global dynamics, connecting fundamental electronic, structural, and chemical dynamics with the collective phenomena of extended systems.[182] Emerging exceptionally powerful X-ray spectroscopy methods such as X-ray photon correlation spectroscopy (XPCS),[183] and resonant inelastic X-ray scattering (RIXS)[184] with sub-natural line width, as demonstrated recently to elucidate structure of water,[185] heroic at 3rd generation light sources, should become routine at DLSRs. We seek to implement these methods at the chemical dynamics beamline. Moving beyond our own narrow confines, we will incorporate methods and techniques being developed by synchrotron scientists[186-190] to probe the photons, ions, and electrons that occur upon irradiation of X-rays in a liquid environment. A challenge and opportunity would be to incorporate mass spectrometry, that has worked so well for us in the VUV region, to probe aqueous systems and nanoparticles in the soft X-ray region. We at Berkeley,[191] among others are beginning to use ambient ionization mass spectrometry to probe drops and aerosols, and one can begin to couple these systems with soft X-ray spectroscopy. Our own vision includes mobile end-stations coupled to high repetition lasers, and development of novel sources that will usher in a new paradigm of probing length and time scales, essentially structure and dynamics, of relevance in Physical Chemistry and Chemical Physics.

Acknowledgements

The authors are indebted to all our co-workers for the work presented here (Bo Xu, Biswajit Bandyopadhyay, Wenchao Lu, Tyler Troy, Yigang Fang, Amir Golan, Chao Ruan, Tamar Stein, Francesca Bell, Martin Head-Gordon, Alexandre Barrozo, Anastasia Gunina, Anna Krylov, Oliver Gessner and Michael Jacobs). We benefit enormously from the close collaboration with our colleague Kevin Wilson in our aerosol and nanoparticle endeavors at the Chemical Dynamics Beamline. We are grateful to Selim Alayoglu, and Daniel J. Rosenberg, for providing figures, materials and valuable discussions regarding silica and confinement. The authors gratefully acknowledge support from the Director, Office of Energy Research, Office of Basic Energy Sciences, Chemical Sciences Division of the U.S. Department of Energy under contract No. DE-AC02-05CH1123, through the Gas Phase Chemical Physics program and Condensed Phase Interfaces and Molecular Sciences program for the cluster and nanoparticle work respectively. The ALS is supported through the same contract.

References

1. O. Kostko, B. Bandyopadhyay and M. Ahmed, *Annu. Rev. Phys. Chem.*, 2016, **67**, 19-40.
2. S. R. Leone, M. Ahmed and K. R. Wilson, *Phys. Chem. Chem. Phys.*, 2010, **12**, 6564-6578.
3. D. S. Peterka and M. Ahmed, *Synchrotron Radiat. News*, 2005, **18**, 35-37.
4. M. Hochlaf, *Phys. Chem. Chem. Phys.*, 2017, **19**, 21236-21261.
5. P. M. Kraus, M. Zürch, S. K. Cushing, D. M. Neumark and S. R. Leone, *Nat. Rev. Chem.*, 2018, **2**, 82-94.
6. J. Rossbach, J. R. Schneider and W. Wurth, *Phys.Rep.*, 2019, **808**, 1-74.
7. C. Nicolas, J. N. Shu, D. S. Peterka, M. Hochlaf, L. Poisson, S. R. Leone and M. Ahmed, *J. Am. Chem. Soc.*, 2006, **128**, 220-226.
8. A. Golan and M. Ahmed, *Jove-J. Vis. Exp.*, 2012, e50164.
9. R. B. Metz, G. Altinay, O. Kostko and M. Ahmed, *J. Phys. Chem. A*, 2019, **123**, 2194-2202.
10. M. Perera, R. B. Metz, O. Kostko and M. Ahmed, *Angew. Chem.*, 2013, **52**, 888-891.
11. R. I. Kaiser, B. J. Sun, H. M. Lin, A. H. H. Chang, A. M. Mebel, O. Kostko and M. Ahmed, *Astrophys. J.*, 2010, **719**, 1884-1889.
12. R. I. Kaiser, P. Maksyutenko, C. Ennis, F. T. Zhang, X. B. Gu, S. P. Krishtal, A. M. Mebel, O. Kostko and M. Ahmed, *Faraday. Discuss.*, 2010, **147**, 429-478.
13. O. Kostko, M. Ahmed and R. B. Metz, *J. Phys. Chem. A*, 2009, **113**, 1225-1230.
14. D. S. N. Parker, R. I. Kaiser, T. P. Troy and M. Ahmed, *Angew. Chem.*, 2014, **53**, 7740-7744.
15. D. S. N. Parker, R. I. Kaiser, B. Bandyopadhyay, O. Kostko, T. P. Troy and M. Ahmed, *Angew. Chem.*, 2015, **54**, 5421-5424.
16. T. Yang, T. P. Troy, B. Xu, O. Kostko, M. Ahmed, A. M. Mebel and R. I. Kaiser, *Angew. Chem.*, 2016, **55**, 14983-14987.
17. T. Yang, R. I. Kaiser, T. P. Troy, B. Xu, O. Kostko, M. Ahmed, A. M. Mebel, M. V. Zagidullin and V. N. Azyazov, *Angew. Chem.*, 2017, **56**, 4515-4519.
18. L. Zhao, R. I. Kaiser, B. Xu, U. Ablikim, M. Ahmed, M. M. Evseev, E. K. Bashkirov, V. N. Azyazov and A. M. Mebel, *Nat. Astron.*, 2018, **2**, 973-979.
19. L. Zhao, R. I. Kaiser, B. Xu, U. Ablikim, M. Ahmed, D. Joshi, G. Veber, F. R. Fischer and A. M. Mebel, *Nat. Astron.*, 2018, **2**, 413-419.
20. L. Zhao, R. I. Kaiser, W. C. Lu, B. Xu, M. Ahmed, A. N. Morozov, A. M. Mebel, A. H. Howlader and S. F. Wnuk, *Nat. Commun.*, 2019, **10**, 3689.
21. L. Zhao, R. I. Kaiser, B. Xu, U. Ablikim, W. C. Lu, M. Ahmed, M. M. Evseev, E. K. Bashkirov, V. N. Azyazov, M. V. Zagidullin, A. N. Morozov, A. H. Howlader, S. F. Wnuk, A. M. Mebel, D. Joshi, G. Veber and F. R. Fischer, *Nat. Commun.*, 2019, **10**, 1510.
22. L. Zhao, M. Prendergast, R. I. Kaiser, B. Xu, U. Ablikim, M. Ahmed, B.-J. Sun, Y.-L. Chen, A. H. H. Chang, R. K. Mohamed and F. R. Fischer, *Angew. Chem.*, 2019, **58**, 17442-17450.
23. P. T. Lynch, T. P. Troy, M. Ahmed and R. S. Tranter, *Anal. Chem.*, 2015, **87**, 2345-2352.
24. B. Bandyopadhyay, O. Kostko, Y. Fang and M. Ahmed, *J. Phys. Chem. A.*, 2015, **119**, 4083-4092.
25. R. Komorek, B. Xu, J. Yao, U. Ablikim, T. P. Troy, O. Kostko, M. Ahmed and X. Y. Yu, *Rev. Sci. Instrum.*, 2018, **89**, 115105.
26. J. Yao, D. B. Lao, X. Sui, Y. Zhou, S. K. Nune, X. Ma, T. P. Troy, M. Ahmed, Z. Zhu, D. J. Heldebrant and X. Y. Yu, *Phys. Chem. Chem. Phys.*, 2017, **19**, 22627-22632.
27. K. R. Wilson, M. Jimenez-Cruz, C. Nicolas, L. Belau, S. R. Leone and M. Ahmed, *J. Phys. Chem. A*, 2006, **110**, 2106-2113.
28. S. A. Skeen, H. A. Michelsen, K. R. Wilson, D. M. Popolan, A. Violi and N. Hansen, *J. Aerosol Sci.*, 2013, **58**, 86-102.
29. K. O. Johansson, M. P. Head-Gordon, P. E. Schrader, K. R. Wilson and H. A. Michelsen, *Science*, 2018, **361**, 997-1000.

30. K. R. Wilson, D. S. Peterka, M. Jimenez-Cruz, S. R. Leone and M. Ahmed, *Phys. Chem. Chem. Phys.*, 2006, **8**, 1884-1890.
31. O. Kostko, B. Xu, M. I. Jacobs and M. Ahmed, *J. Chem. Phys.*, 2017, **147**, 013931.
32. J. N. Shu, K. R. Wilson, A. N. Arrowsmith, M. Ahmed and S. R. Leone, *Nano. Lett.*, 2005, **5**, 1009-1015.
33. H. J. Zeng, N. Yang and M. A. Johnson, *Faraday. Discuss.*, 2019, **217**, 8-33.
34. M. Farnik and J. Lengyel, *Mass Spectrom. Rev.*, 2018, **37**, 630-651.
35. V. Vaida, *J. Chem. Phys.*, 2011, **135**, 020901.
36. O. Dopfer and M. Fujii, *Chem. Rev.*, 2016, **116**, 5432-5463.
37. H. Schwarz, *Catal. Sci. Technol.*, 2017, **7**, 4302-4314.
38. M. Juanes, R. T. Saragi, W. Caminati and A. Lesarri, *Chem.-Eur. J.*, 2019, **25**, 11402-11411.
39. E. Jimenez-Izal and A. N. Alexandrova, *Annu. Rev. Phys.Chem.*, 2018, **69**, 377-400.
40. J. Yao, D. B. Lao, X. Sui, Y. F. Zhou, S. K. Nune, X. Ma, T. P. Troy, M. Ahmed, Z. H. Zhu, D. J. Heldebrant and X. Y. Yu, *Phys. Chem. Chem. Phys.*, 2017, **19**, 22627-22632.
41. G.-L. Hou, W. Lin and X.-B. Wang, *Comm. Chem.*, 2018, **1**, 37.
42. B. E. Wyslouzil and J. Wolk, *J. Chem. Phys.*, 2016, **145**, 211702.
43. J. Kirkby, J. Duplissy, K. Sengupta, C. Frege, H. Gordon, C. Williamson, M. Heinritzi, M. Simon, C. Yan, J. Almeida, J. Trostl, T. Nieminen, I. K. Ortega, R. Wagner, A. Adamov, A. Amorim, A. K. Bernhammer, F. Bianchi, M. Breitenlechner, S. Brilke, X. Chen, J. Craven, A. Dias, S. Ehrhart, R. C. Flagan, A. Franchin, C. Fuchs, R. Guida, J. Hakala, C. R. Hoyle, T. Jokinen, H. Junninen, J. Kangasluoma, J. Kim, M. Krapf, A. Kurten, A. Laaksonen, K. Lehtipalo, V. Makhmutov, S. Mathot, U. Molteni, A. Onnela, O. Perakyla, F. Piel, T. Petaja, A. P. Praplan, K. Pringle, A. Rap, N. A. Richards, I. Riipinen, M. P. Rissanen, L. Rondo, N. Sarnela, S. Schobesberger, C. E. Scott, J. H. Seinfeld, M. Sipila, G. Steiner, Y. Stozhkov, F. Stratmann, A. Tome, A. Virtanen, A. L. Vogel, A. C. Wagner, P. E. Wagner, E. Weingartner, D. Wimmer, P. M. Winkler, P. Ye, X. Zhang, A. Hansel, J. Dommen, N. M. Donahue, D. R. Worsnop, U. Baltensperger, M. Kulmala, K. S. Carslaw and J. Curtius, *Nature*, 2016, **533**, 521-526.
44. O. Kostko, L. Belau, K. R. Wilson and M. Ahmed, *J. Phys. Chem. A*, 2008, **112**, 9555-9562.
45. A. Lietard and J. R. R. Verlet, *J. Phys. Chem. Lett.*, 2019, **10**, 1180-1184.
46. M. S. El-Shall, *Accounts Chem. Res.*, 2008, **41**, 783-792.
47. R. I. Kaiser, D. S. N. Parker and A. M. Mebel, *Annu. Rev. Phys.Chem.*, 2015, **66**, 43-67.
48. L. Zhao, R. I. Kaiser, B. Xu, U. Ablikim, M. Ahmed, M. V. Zagidullin, V. N. Azyazov, A. H. Howlader, S. F. Wnuk and A. M. Mebel, *J. Phys. Chem. Lett.*, 2018, **9**, 2620-2626.
49. K. Kohse-Hoinghaus, *Pure Appl. Chem.*, 2019, **91**, 271-288.
50. E. S. Agudosi, E. C. Abdullah, A. Numan, N. M. Mubarak, M. Khalid and N. Omar, *Crit Rev Solid State*, 2019.
51. M. A. Majewski and M. Stepien, *Angew. Chem.*, 2019, **58**, 86-116.
52. Y. Segawa, H. Ito and K. Itami, *Nat. Rev. Mater.*, 2016, **1**, 15002.
53. B. Bandyopadhyay, T. Stein, Y. Fang, O. Kostko, A. White, M. Head-Gordon and M. Ahmed, *J. Phys. Chem. A.*, 2016, **120**, 5053-5064.
54. T. Stein, B. Bandyopadhyay, T. P. Troy, Y. Fang, O. Kostko, M. Ahmed and M. Head-Gordon, *P. Natl. Acad. Sci. USA*, 2017, **114**, 4125-4133.
55. P. V. Schleyer, H. J. Jiao, M. N. Glukhovtsev, J. Chandrasekhar and E. Kraka, *J. Am. Chem. Soc.*, 1994, **116**, 10129-10134.
56. R. Peverati, P. P. Bera, T. J. Lee and M. Head-Gordon, *J. Phys. Chem. A.*, 2014, **118**, 10109-10116.
57. Y. Matsuda, N. Mikami and A. Fujii, *Phys. Chem. Chem. Phys.*, 2009, **11**, 1279-1290.
58. H. Hopf, in *Modern Arene Chemistry*, ed. D. Astruc, Wiley-VCH, Weinheim, Germany2004, pp. 169-195.
59. Y. Ono and C. Y. Ng, *J. Am. Chem. Soc.*, 1982, **104**, 4752-4758.
60. J. A. Booze and T. Baer, *J. Chem. Phys.*, 1993, **98**, 186-200.

61. M. T. Coolbaugh, S. G. Whitney, G. Vaidyanathan and J. F. Garvey, *J. Phys. Chem.*, 1992, **96**, 9139-9144.
62. P. O. Momoh, S. A. Abrash, R. Mabrouki and M. S. El-Shall, *J. Am. Chem. Soc.*, 2006, **128**, 12408-12409.
63. P. O. Momoh and M. S. El-Shall, *Chem. Phys. Lett.*, 2007, **436**, 25-29.
64. R. A. Relph, J. C. Bopp, J. R. Roscioli and M. A. Johnson, *J. Chem. Phys.*, 2009, **131**.
65. N. J. Van Zee, B. Adelizzi, M. F. J. Mabesoone, X. Meng, A. Aloi, R. H. Zha, M. Lutz, I. A. W. Filot, A. R. A. Palmans and E. W. Meijer, *Nature*, 2018, **558**, 100-103.
66. M. P. van Der Helm, B. Klemm and R. Eelkema, *Nat. Rev. Chem.*, 2019, **3**, 491-508.
67. S. Serrano-Luginbuhl, K. Ruiz-Mirazo, R. Ostaszewski, F. Gallou and P. Walde, *Nat. Rev. Chem.*, 2018, **2**, 306-327.
68. S. Whitelam and R. L. Jack, *Annu. Rev. Phys.Chem.*, 2015, **66**, 143-163.
69. X. Lou, R. P. M. Lafleur, C. M. A. Leenders, S. M. C. Schoenmakers, N. M. Matsumoto, M. B. Baker, J. L. J. van Dongen, A. R. A. Palmans and E. W. Meijer, *Nat. Commun.*, 2017, **8**, 15420.
70. E. Kamarchik, O. Kostko, J. M. Bowman, M. Ahmed and A. I. Krylov, *J. Chem. Phys.*, 2010, **132**, 194311.
71. K. B. Bravaya, O. Kostko, M. Ahmed and A. I. Krylov, *Phys. Chem. Chem. Phys.*, 2010, **12**, 2292-2307.
72. O. Kostko, K. Bravaya, A. Krylov and M. Ahmed, *Phys. Chem. Chem. Phys.*, 2010, **12**, 2860-2872.
73. A. Golan, K. B. Bravaya, R. Kudirka, O. Kostko, S. R. Leone, A. I. Krylov and M. Ahmed, *Nat. Chem.*, 2012, **4**, 323-329.
74. K. Khistyaev, K. B. Bravaya, E. Kamarchik, O. Kostko, M. Ahmed and A. I. Krylov, *Faraday. Discuss.*, 2011, **150**, 313-330.
75. K. Khistyaev, A. Golan, K. B. Bravaya, N. Orms, A. I. Krylov and M. Ahmed, *J. Phys. Chem. A.*, 2013, **117**, 6789-6797.
76. P. Ball, *Proc. Nat. Acad. Sci.*, 2017, **114**, 13327-13335.
77. J. Bouwman, D. M. Paardekooper, H. M. Cuppen, H. Linnartz and L. J. Allamandola, *Astrophys. J.*, 2009, **700**, 56-62.
78. M. Meot-Ner, *Chem. Rev.*, 2012, **112**, Rp22-Rp103.
79. J. J. Towey, A. K. Soper and L. Dougan, *J. Phys. Chem. B.*, 2016, **120**, 4439-4448.
80. A. V. Egorov, A. P. Lyubartsev and A. Laaksonen, *J. Phys. Chem. B.*, 2011, **115**, 14572-14581.
81. E. Shalaev, A. Soper, J. A. Zeitler, S. Ohtake, C. J. Roberts, M. J. Pikal, K. Wu and E. Boldyreva, *J. Pharm. Sci.*, 2019, **108**, 36-49.
82. F. Bell, Q. N. Ruan, A. Golan, P. R. Horn, M. Ahmed, S. R. Leone and M. Head-Gordon, *J. Am. Chem. Soc.*, 2013, **135**, 14229-14239.
83. D. Ghosh, A. Golan, L. K. Takahashi, A. I. Krylov and M. Ahmed, *J. Phys. Chem. Lett.*, 2012, **3**, 97-101.
84. P. R. Horn, Y. Mao and M. Head-Gordon, *Phys. Chem. Chem. Phys.*, 2016, **18**, 23067-23079.
85. T. Miyake and M. Rolandi, in *Green Materials for Electronics*, Wiley-VCH2017, pp. 235-253.
86. N. Agmon, H. J. Bakker, R. K. Campen, R. H. Henchman, P. Pohl, S. Roke, M. Thämer and A. Hassanali, *Chem. Rev.*, 2016, **116**, 7642-7672.
87. K. Gopinadhan, S. Hu, A. Esfandiar, M. Lozada-Hidalgo, F. C. Wang, Q. Yang, A. V. Tyurnina, A. Keerthi, B. Radha and A. K. Geim, *Science*, 2019, **363**, 145-148.
88. O. Kostko, T. P. Troy, B. Bandyopadhyay and M. Ahmed, *Phys. Chem. Chem. Phys.*, 2016, **18**, 25569-25573.
89. J. Postulka, P. Slavicek, A. Domaracka, A. Pysanenko, M. Farnik and J. Kocisek, *Phys. Chem. Chem. Phys.*, 2019, **21**, 13925-13933.
90. K. Grygoryeva, M. Oncak, A. Pysanenko and M. Farnik, *Phys. Chem. Chem. Phys.*, 2019, **21**, 8221-8227.
91. K. I. Oberg, *Chem. Rev.*, 2016, **116**, 9631-9663.

92. A. Courty, M. Mons, J. LeCalve, F. Piuzzi and I. Dimicoli, *J. Phys. Chem. A*, 1997, **101**, 1445-1450.
93. M. Mons, I. Dimicoli and F. Piuzzi, *Int. Rev. Phys. Chem.*, 2002, **21**, 101-135.
94. M. Miyazaki, A. Fujii, T. Ebata and N. Mikami, *J. Phys. Chem. A*, 2004, **108**, 10656-10660.
95. M. Miyazaki, A. Fujii, T. Ebata and N. Mikami, *Chem. Phys. Lett.*, 2004, **399**, 412-416.
96. M. Miyazaki, A. Fujii and N. Mikami, *J. Phys. Chem. A*, 2004, **108**, 8269-8272.
97. Y. M. Ibrahim, M. M. N. Mautner, E. H. Alshraeh, M. S. El-Shall and S. Scheiner, *J. Am. Chem. Soc.*, 2005, **127**, 7053-7064.
98. A. K. Lemmens, S. Gruet, A. L. Steber, J. Antony, S. Grimme, M. Schnell and A. M. Rijs, *Phys. Chem. Chem. Phys.*, 2019, **21**, 3414-3422.
99. K. Chatterjee and O. Dopfer, *Chem. Sci.*, 2018, **9**, 2301-2318.
100. K. Chatterjee and O. Dopfer, *Phys. Chem. Chem. Phys.*, 2017, **19**, 32262-32271.
101. M. S. Gudipati and L. J. Allamandola, *Astrophys. J.*, 2004, **615**, 177-180.
102. S. H. Cuylle, L. J. Allamandola and H. Linnartz, *Astron. Astrophys.*, 2014, **562**, A22-29.
103. B. Radha, A. Esfandiar, F. C. Wang, A. P. Rooney, K. Gopinadhan, A. Keerthi, A. Mishchenko, A. Janardanan, P. Blake, L. Fumagalli, M. Lozada-Hidalgo, S. Garaj, S. J. Haigh, I. V. Grigorieva, H. A. Wu and A. K. Geim, *Nature*, 2016, **538**, 222-225.
104. A. Striolo, A. Michaelides and L. Joly, *Annu. Rev. Chem. Biomol.*, 2016, **7**, 533-556.
105. B. Xu, T. Stein, U. Ablikim, L. Jiang, J. Hendrix, M. Head-Gordon and M. Ahmed, *Faraday. Discuss.*, 2019, 414-433.
106. D. Wang and A. Fujii, *Chem. Sci.*, 2017, **8**, 2667-2670.
107. M. Xie, H. R. Tsai, A. Fujii and Y. P. Lee, *Phys. Chem. Chem. Phys.*, 2019, **21**, 16055-16063.
108. C. Joblin, L. Dontot, G. A. Garcia, F. Spiegelman, M. Rapacioli, L. Nahon, P. Parneix, T. Pino and P. Brechignac, *J. Phys. Chem. Lett.*, 2017, **8**, 3697-3702.
109. S. Hartweg, B. L. Yoder, G. A. Garcia, L. Nahon and R. Signorell, *Phys. Rev. Lett.*, 2017, **118**, 103402.
110. L. Belau, K. R. Wilson, S. R. Leone and M. Ahmed, *J. Phys. Chem. A*, 2007, **111**, 10075-10083.
111. G. Niedner-Schatteburg and V. E. Bondybey, *Chem. Rev.*, 2000, **100**, 4059-4086.
112. B. Brutschy, *Chem. Rev.*, 1992, **92**, 1567-1587.
113. Y. Nakai, H. Hidaka, N. Watanabe and T. M. Kojima, *J. Chem. Phys.*, 2016, **144**, 224306.
114. Y. Nagata, K. Usui and M. Bonn, *Phys. Rev. Lett.*, 2015, **115**.
115. H. Abdoul-Carime, F. Berthias, L. Feketeova, M. Marciante, F. Calvo, V. Forquet, H. Chermette, B. Farizon, M. Farizon and T. D. Mark, *Angew. Chem.*, 2015, **54**, 14685-14689.
116. Z.-H. Loh, G. Doumy, C. Arnold, L. Kjellsson, S. W. Southworth, A. A. Haddad, Y. Kumagai, M.-F. Tu, P. J. Ho, A. M. March, R. D. Schaller, M. S. Bin Mohd Yusof, T. Debnath, M. Simon, R. Welsch, L. Inhester, K. Khalili, K. Nanda, A. I. Krylov, S. Moeller, G. Coslovich, J. Koralek, M. P. Minitti, W. F. Schlotter, J. -E. Rubensson, R. Santra and L. Young, *Science*, 2020, **367,** 179-182.
117. B. D. Adamson, S. A. Skeen, M. Ahmed and N. Hansen, *J. Phys. Chem. A.*, 2018, **122**, 9338-9349.
118. C. Richter, D. Hollas, C. M. Saak, M. Forstel, T. Miteva, M. Mucke, O. Bjorneholm, N. Sisourat, P. Slavicek and U. Hergenhahn, *Nat. Commun.*, 2018, **9**, 4988.
119. J. Ullrich, R. Moshammer, R. Dörner, O. Jagutzki, V. Mergel, H. Schmidt-Böcking and L. Spielberger, *J. Phys. B*, 1997, **30**, 2917-2974.
120. S. Marburger, O. Kugeler, U. Hergenhahn and T. Möller, *Phys. Rev. Lett.*, 2003, **90**, 203401.
121. G. D. Scholes, *Faraday. Discuss.*, 2020, **221**, 265-280.
122. Ö. Şahin, İ. Tapan, E. N. Özmutlu and R. Veenhof, *J. Instrum.*, 2010, **5**, P05002.
123. A. Golan and M. Ahmed, *J. Phys. Chem. Lett.*, 2012, **3**, 458-462.
124. J. Kocisek, J. Lengyel, M. Farnik and P. Slavicek, *J. Chem. Phys.*, 2013, **139**, 214308.
125. O. Svoboda, M. Oncak and P. Slavicek, *J. Chem. Phys.*, 2011, **135**, 154301.
126. D. M. Chipman, *J. Chem. Phys.*, 2005, **122**, 44111.

127. Y. Yoshimura, N. A. Oktaviani, K. Yonezawa, H. Kamikubo and F. A. A. Mulder, *Angew. Chem.*, 2017, **56**, 239-242.
128. L. B. Li, I. Vorobyov and T. W. Allen, *J. Phys. Chem. B.*, 2013, **117**, 11906-11920.
129. M. Kellermeier, R. Rosenberg, A. Moise, U. Anders, M. Przybylski and H. Colfen, *Faraday. Discuss.*, 2012, **159**, 23-45.
130. A. Barrozo, B. Xu, A. O. Gunina, M. I. Jacobs, K. Wilson, O. Kostko, M. Ahmed and A. I. Krylov, *J. Phys. Chem. Lett.*, 2019, **10**, 1860-1865.
131. P. C. Chang, Y. Yu, Z. H. Wu, P. C. Lin, W. R. Chen, C. C. Su, M. S. Chen, Y. L. Li, T. P. Huang, Y. Y. Lee and C. C. Wang, *J. Phys. Chem. B.*, 2016, **120**, 10181-10191.
132. P. C. Lin, Z. H. Wu, M. S. Chen, Y. L. Li, W. R. Chen, T. P. Huang, Y. Y. Lee and C. C. Wang, *J. Phys. Chem. B.*, 2017, **121**, 1054-1067.
133. B. Xu, M. I. Jacobs, O. Kostko and M. Ahmed, *ChemPhysChem*, 2017, **18**, 1503-1506.
134. R. Seidel, B. Winter and S. E. Bradforth, *Annu. Rev. Phys. Chem.*, 2016, **67**, 283-305.
135. J. W. Smith and R. J. Saykally, *Chem. Rev.*, 2017, **117**, 13909-13934.
136. T. Suzuki, *J. Chem. Phys.*, 2019, **151**, 090901.
137. Y. Zheng and L. Sanche, *Appl. Phys. Rev.*, 2018, **5**, 021302.
138. M. C. Boyer, N. Rivas, A. A. Tran, C. A. Verish and C. R. Arumainayagam, *Surf. Sci.*, 2016, **652**, 26-32.
139. C. R. Arumainayagam, H.-L. Lee, R. B. Nelson, D. R. Haines and R. P. Gunawardane, *Surf. Sci. Rep.*, 2010, **65**, 1-44.
140. D. Luckhaus, Y. I. Yamamoto, T. Suzuki and R. Signorell, *Sci. Adv.*, 2017, **3**, 1603224.
141. D. M. Bartels, *Journal of Physical Chemistry Letters*, 2019, **10**, 4910-4913.
142. M. P. Seah and W. A. Dench, *Surf. Interface. Anal.*, 1979, **1**, 2-11.
143. S. Thurmer, R. Seidel, M. Faubel, W. Eberhardt, J. C. Hemminger, S. E. Bradforth and B. Winter, *Phys. Rev. Lett.*, 2013, **111**, 173005.
144. M. I. Jacobs, O. Kostko, M. Ahmed and K. R. Wilson, *Phys. Chem. Chem. Phys.*, 2017, **19**, 13372-13378.
145. O. Kostko, M. I. Jacobs, B. Xu, K. R. Wilson and M. Ahmed, *J. Chem. Phys.*, 2019, **151**, 9.
146. E. Antonsson, B. Langer, I. Halfpap, J. Gottwald and E. Ruhl, *J. Chem. Phys.*, 2017, **146**, 244301.
147. Y. Suzuki, K. Nishizawa, N. Kurahashi and T. Suzuki, *Phys. Rev. E*, 2014, **90**, 010302.
148. J. Cooper and R. N. Zare, *J. Chem. Phys.*, 1968, **48**, 942-943.
149. M. L. Vidal, A. I. Krylov and S. Coriani, *Phys. Chem. Chem. Phys.*, 2020, DOI:10.1039/C1039CP03695D.
150. T. Fransson, Y. Harada, N. Kosugi, N. A. Besley, B. Winter, J. J. Rehr, L. G. M. Pettersson and A. Nilsson, *Chem. Rev.*, 2016, **116**, 7551-7569.
151. P. Jungwirth and D. J. Tobias, *Chem. Rev.*, 2006, **106**, 1259-1281.
152. J. A. Faust and G. M. Nathanson, *Chem. Soc. Rev.*, 2016, **45**, 3609-3620.
153. D. Gebauer, P. Raiteri, J. D. Gale and H. Colfen, *Am. J. Sci.*, 2018, **318**, 969-988.
154. C. D. Ma, C. X. Wang, C. Acevedo-Velez, S. H. Gellman and N. L. Abbott, *Nature*, 2015, **517**, 347–350.
155. R. Mogaki, P. K. Hashim, K. Okuro and T. Aida, *Chem. Soc. Rev.*, 2017, **46**, 6480-6491.
156. H. D. Herce, A. E. Garcia and M. C. Cardoso, *J. Am. Chem. Soc.*, 2014, **136**, 17459-17467.
157. B. R. Bzdek and J. P. Reid, *J. Chem. Phys.*, 2017, **147**, 220901.
158. A. Virtanen, J. Joutsensaari, T. Koop, J. Kannosto, P. Yli-Pirilä, J. Leskinen, J. M. Mäkelä, J. K. Holopainen, U. Pöschl, M. Kulmala, D. R. Worsnop and A. Laaksonen, *Nature*, 2010, **467**, 824-827.
159. C. M. Roth, K.-U. Goss and R. P. Schwarzenbach, *Environ. Sci. Technol.*, 2005, **39**, 6632-6637.
160. T. Koop, J. Bookhold, M. Shiraiwa and U. Pöschl, *Phys. Chem. Chem. Phys.*, 2011, **13**, 19238-19255.
161. J. P. Reid, A. K. Bertram, D. O. Topping, A. Laskin, S. T. Martin, M. D. Petters, F. D. Pope and G. Rovelli, *Nat. Commun.*, 2018, **9**, 956.

162. M. I. Jacobs, B. Xu, O. Kostko, N. Heine, M. Ahmed and K. R. Wilson, *J. Phys. Chem. A.*, 2016, **120**, 8645-8656.
163. M. I. Jacobs, B. Xu, O. Kostko, A. A. Wiegel, F. A. Houle, M. Ahmed and K. R. Wilson, *J. Phys. Chem. A.*, 2019, **123**, 6034-6044.
164. M. D. Fayer and N. E. Levinger, *Annu. Rev. Anal. Chem.*, 2010, **3**, 89-107.
165. D. J. Rosenberg, S. Alayoglu, R. Kostecki and M. Ahmed, *Nanoscale Adv.*, 2019, **1**, 4878-4887.
166. M. A. Brown, M. Arrigoni, F. Héroguel, A. Beloqui Redondo, L. Giordano, J. A. van Bokhoven and G. Pacchioni, *J. Phys. Chem. C*, 2014, **118**, 29007-29016.
167. M. A. Brown, T. Huthwelker, A. Beloqui Redondo, M. Janousch, M. Faubel, C. A. Arrell, M. Scarongella, M. Chergui and J. A. van Bokhoven, *J. Phys. Chem. Lett.*, 2012, **3**, 231-235.
168. T. A. Gmür, A. Goel and M. A. Brown, *J. Phys. Chem. C*, 2016, **120**, 16617-16625.
169. L. Seiffert, Q. Liu, S. Zherebtsov, A. Trabattoni, P. Rupp, M. C. Castrovilli, M. Galli, F. Süßmann, K. Wintersperger, J. Stierle, G. Sansone, L. Poletto, F. Frassetto, I. Halfpap, V. Mondes, C. Graf, E. Rühl, F. Krausz, M. Nisoli, T. Fennel, F. Calegari and M. F. Kling, *Nat. Phys,*, 2017, **13**, 766-770.
170. B. Gilbert, B. H. Frazer, F. Naab, J. Fournelle, J. W. Valley and G. De Stasio, *Am. Mineral.*, 2003, **88**, 763-769.
171. I. Davoli, E. Paris, S. Stizza, M. Benfatto, M. Fanfoni, A. Gargano, A. Bianconi and F. Seifert, *Phys. Chem. Miner.*, 1992, **19**, 171-175.
172. C. Corder, P. Zhao, J. Bakalis, X. Li, M. D. Kershis, A. R. Muraca, M. G. White and T. K. Allison, *Struc. Dyn.*, 2018, **5**, 054301.
173. V. Paunović, P. Hemberger, A. Bodi, N. López and J. Pérez-Ramírez, *Nat. Catal.*, 2018, **1**, 363-370.
174. M. Chergui and E. Collet, *Chem. Rev.*, 2017, **117**, 11025-11065.
175. S. Neppl, A. Shavorskiy, I. Zegkinoglou, M. Fraund, D. S. Slaughter, T. Troy, M. P. Ziemkiewicz, M. Ahmed, S. Gul, B. Rude, J. Z. Zhang, A. S. Tremsin, P. A. Glans, Y. S. Liu, C. H. Wu, J. H. Guo, M. Salmeron, H. Bluhm and O. Gessner, *Faraday. Discuss.*, 2014, **171**, 219-241.
176. J. Mahl, S. Neppl, F. Roth, M. Borgwardt, C. Saladrigas, B. Toulson, J. Cooper, T. Rahman, H. Bluhm, J. H. Guo, W. L. Yang, N. Huse, W. Eberhardt and O. Gessner, *Faraday. Discuss.*, 2019, **216**, 414-433.
177. F. Roth, S. Neppl, A. Shavorskiy, T. Arion, J. Mahl, H. O. Seo, H. Bluhm, Z. Hussain, O. Gessner and W. Eberhardt, *Phys Rev B*, 2019, **99**, 020303.
178. W. Xiong, D. D. Hickstein, K. J. Schnitzenbaumer, J. L. Ellis, B. B. Palm, K. E. Keister, C. Y. Ding, L. Miaja-Avila, G. Dukovic, J. L. Jimenez, M. M. Murnane and H. C. Kapteyn, *Nano. Lett.*, 2013, **13**, 2924-2930.
179. J. L. Ellis, D. D. Hickstein, K. J. Schnitzenbaumer, M. B. Wilker, B. B. Palm, J. L. Jimenez, G. Dukovic, H. C. Kapteyn, M. M. Murnane and W. Xiong, *J. Am. Chem. Soc.*, 2015, **137**, 3759-3762.
180. S. Nemsak, E. Strelcov, T. Duchon, H. Guo, J. Hackl, A. Yulaev, I. Vlassiouk, D. N. Mueller, C. M. Schneider and A. Kolmakov, *J. Am. Chem. Soc.*, 2017, **139**, 18138-18141.
181. M. Eriksson, J. F. van der Veen and C. Quitmann, *J. Synchrotron Radiat.*, 2014, **21**, 837-842.
182. https://als.lbl.gov/wp-content/uploads/2017/08/ALS-U-Early-Science-Workshop-Report-Full.pdf.
183. F. Perakis, K. Amann-Winkel, F. Lehmkuhler, M. Sprung, D. Mariedahl, J. A. Sellberg, H. Pathak, A. Spah, F. Cavalca, D. Schlesinger, A. Ricci, A. Jain, B. Massani, F. Aubree, C. J. Benmore, T. Loerting, G. Grubel, L. G. M. Pettersson and A. Nilsson, *P. Natl. Acad. Sci. USA*, 2017, **114**, 8193-8198.
184. J. Niskanen, M. Fondell, C. J. Sahle, S. Eckert, R. M. Jay, K. Gilmore, A. Pietzsch, M. Dantz, X. Y. Lu, D. E. McNally, T. Schmitt, V. V. da Cruz, V. Kimberg, F. Gel'mukhanov and A. Fohlisch, *P. Natl. Acad. Sci. USA*, 2019, **116**, 4058-4063.

185. V. Vaz da Cruz, F. Gel'mukhanov, S. Eckert, M. Iannuzzi, E. Ertan, A. Pietzsch, R. C. Couto, J. Niskanen, M. Fondell, M. Dantz, T. Schmitt, X. Lu, D. McNally, R. M. Jay, V. Kimberg, A. Föhlisch and M. Odelius, *Nat. Commun.*, 2019, **10**, 1013.
186. F. Meyer, M. Blum, A. Benkert, D. Hauschild, Y. L. Jeyachandran, R. G. Wilks, W. Yang, M. Bar, F. Reinert, C. Heske, M. Zharnikov and L. Weinhardt, *Phys. Chem. Chem. Phys.*, 2018, **20**, 8302-8310.
187. M. Favaro, B. Jeong, P. N. Ross, J. Yano, Z. Hussain, Z. Liu and E. J. Crumlin, *Nat. Commun.*, 2016, **7**, 12695.
188. J. D. Koralek, J. B. Kim, P. Bruza, C. B. Curry, Z. J. Chen, H. A. Bechtel, A. A. Cordones, P. Sperling, S. Toleikis, J. F. Kern, S. P. Moeller, S. H. Glenzer and D. P. DePonte, *Nat. Commun.*, 2018, **9**, 1353
189. Y. H. Lu, J. M. Larson, A. Baskin, X. Zhao, P. D. Ashby, D. Prendergast, H. A. Bechtel, R. Kostecki and M. Salmeron, *Nano. Lett.*, 2019, **19**, 5388-5393.
190. S. Nemsak, E. Strelcov, H. X. Guo, B. D. Hoskins, T. Duchon, D. N. Mueller, A. Yulaev, I. Vlassiouk, A. Tselev, C. M. Schneider and A. Kolmakov, *Top. Catal.*, 2018, **61**, 2195-2206.
191. J. F. Davies and K. R. Wilson, *Chem. Sci.*, 2015, **6**, 7020-7027.

TOC entry: Synchrotron radiation provides insight into spectroscopy and dynamics in clusters and nanoparticles.